EVI-SAM: Robust, Real-time, Tightly-coupled Event-Visual-Inertial State Estimation and 3D Dense Mapping

Weipeng Guan, Peiyu Chen, Huibin Zhao, Yu Wang, Peng Lu*

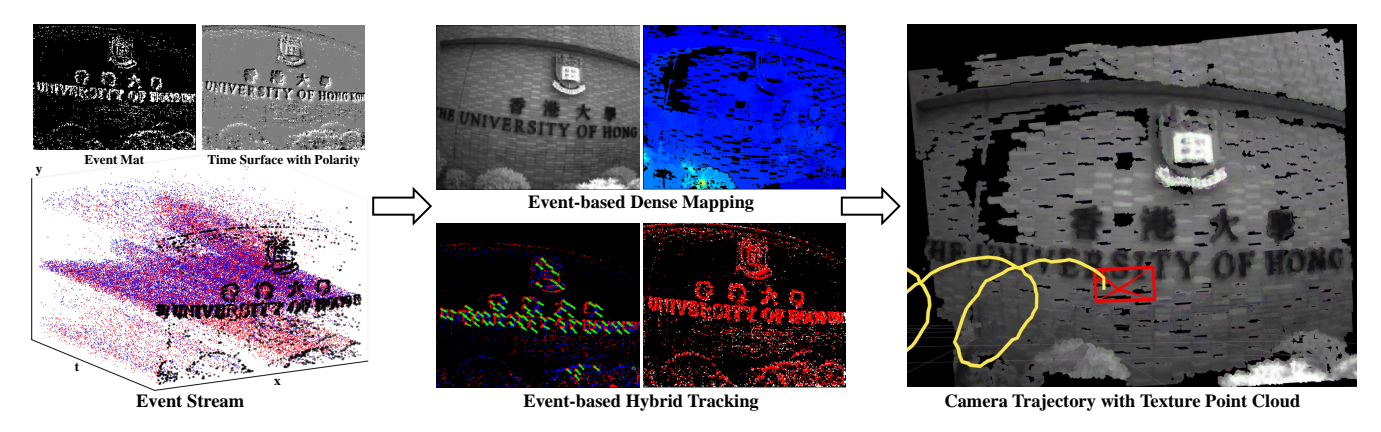


Fig. 1. Our EVI-SAM enables the recovery of both the camera pose and dense maps of the scene. The tracking module leverages the reprojection constraint from the feature-based method and the relative pose constraints from the direct-based method within an event-based hybrid tracking framework. The mapping module represents a pioneering event-based dense mapping framework, distinguished as a non-learning method that can conduct real-time dense and texture mapping on a standard CPU.

Abstract-Event cameras are bio-inspired, motion-activated sensors that demonstrate substantial potential in handling challenging situations, such as motion blur and high-dynamic range. In this paper, we proposed EVI-SAM to tackle the problem of 6 DoF pose tracking and 3D reconstruction using monocular event camera. A novel event-based hybrid tracking framework is designed to estimate the pose, leveraging the robustness of feature matching and the precision of direct alignment. Specifically, we develop an event-based 2D-2D alignment to construct the photometric constraint, and tightly integrate it with the event-based reprojection constraint. The mapping module recovers the dense and colorful depth of the scene through the image-guided event-based mapping method. Subsequently, the appearance, texture, and surface mesh of the 3D scene can be reconstructed by fusing the dense depth map from multiple viewpoints using truncated signed distance function (TSDF) fusion. To the best of our knowledge, this is the first non-learning work to realize event-based dense mapping. Numerical evaluations are performed on both publicly available and self-collected datasets, which qualitatively and quantitatively demonstrate the superior performance of our method. Our EVI-SAM effectively balances accuracy and robustness while maintaining computational efficiency, showcasing superior pose tracking and dense mapping performance in challenging scenarios. Video Demo: https://youtu.be/Nn40U4e5Si8.

Index Terms—Event-based Vision, 6-DoF Pose Tracking, 3D Dense Mapping, SLAM, Robotics.

The authors are with the Adaptive Robotic Controls Lab (ArcLab), Department of Mechanical Engineering, The University of Hong Kong, Hong Kong SAR, China. E-mail: {wpguan, chenpyhk, hbzhao, ywang812}@connect.hku.hk, lupeng@hku.hk.

This work was supported by General Research Fund under Grant 17204222, and in part by the Seed Fund for Collaborative Research and General Funding Scheme-HKU-TCL Joint Research Center for Artificial Intelligence.

I. INTRODUCTION

A. Motivations

E VENT camera captures high-quality data either in extreme lighting scenes or high-speed motion, which paves the way to tackle challenging scenarios in robotics such as Visual Odometry (VO), Visual Inertial Odometry (VIO), Simultaneous Localization and Mapping (SLAM), etc. This novel sensor offers many advantages over standard cameras including high temporal resolutions (μ s-level), high dynamic range (HDR, 140 dB), low power consumption, and immunity to motion blur [1]. However, the event camera exclusively responds to moving edges within the scene, inherently resulting in sparse and asynchronous output. This poses a challenge in the estimation of dense depth and the recovery of detailed structures for objects and environments, especially in low-contrast regions where events may not be triggered.

Previous works in event-based depth estimation, such as EMVS [2] and Ref. [3] [4], have shown impressive performance in sparse or semi-dense mapping, while event-based dense mapping using non-learning methods remains a research gap. Learning-based approaches for event-based dense mapping are present in [5]–[10], which rely on extensive training data and provide no guarantees of optimality or generality. Additionally, these approaches can only produce local depth maps and are incapable of reconstructing a globally consistent depth map. How to effectively exploit the sparse spatial information and abundant temporal cues from asynchronous events to generate dense depth maps remains an unsolved problem. This motivates us to investigate the

 $^{^{*}}$ corresponding author;

complementarity between events and images, exploring the event-based dense mapping approach for inferring dense depth from sparse and incomplete event measurements.

Meanwhile, event-based pose tracking has also gained significant research interest for challenging scenarios where the performance of traditional cameras may be compromised such as under extreme lighting conditions and very fast motion. Prior studies on event-based pose tracking using direct-based methods (such as EVO [11], ESVO [12], EDS [13]) as well as feature-based methods (such as Ultimate-SLAM [14], PL-EVIO [15], ESVIO [16]) has made significant progress in state estimation, while they are still in early stages. Besides, both feature-based and direct-based methods have their strengths and weaknesses in their respective aspects, contributing to mutual complementarity to some degree. Exploring how to better leverage or integrate the respective advantages of feature-based methods and directbased methods for event-based pose tracking remains an uncharted area. This motivates us to combine feature-based and direct methods for a more robust and accurate eventbased pose tracker.

B. Contributions

In this work, we introduce the EVI-SAM, a comprehensive SLAM system that integrates events, images, and IMU data seamlessly. To this end, an event-based hybrid tracking pipeline is designed to enable accurate 6-DoF pose tracking and an event-based dense mapping method is proposed to reconstruct the dense depth of the surrounding environment. To the best of our knowledge, this is the first framework that employs a non-learning approach to achieve event-based dense and textured 3D reconstruction without GPU acceleration. Additionally, it is also the first hybrid approach that integrates both photometric and geometric errors within an event-based framework. Our contributions can be summarized as follows:

- 1) We present a novel direct event-based pose tracking scheme that employs event-based 2D-2D alignment for photometric optimization.
- 2) We introduce an innovative event-based hybrid tracking pipeline. This pipeline efficiently constructs a nonlinear graph optimization framework to jointly incorporate the reprojection constraint from the feature-based method and the relative pose constraints from the direct-based method.
- 3) We proposed an event-based dense mapping method. It involves segmenting the event-based semi-dense depth map with image guidance and introduces a novel interpolation method to recover dense depth within each segment. Additionally, we also leverage image measurements to render texture to the map (i.e., the color of 3D points).
- 4) We designed a TSDF-based map fusion method to integrate local event-based depth, producing a precise and globally consistent 3D map that includes appearance and surface mesh.

 Extensive experimental evaluations, both qualitative and quantitative, demonstrate the accuracy, robustness, generalization ability, and outstanding performance of our approach.

The remainder of the paper is organized as follows: Section II introduces the related works on event-based pose tracking and depth estimation. Section III provides a brief overview of our EVI-SAM system, with detailed descriptions of its event-based hybrid tracking and event-based dense mapping presented in Sections IV and V, respectively. Section VI presents the evaluations. Finally, the conclusion is given in Section VII.

II. RELATED WORKS

A. Event-based Pose Tracking

Event-based pose tracking can be classified into two primary categories: (i) feature/indirect-based methods [14]–[16], that extract a sparse set of repeatable event-based features from the event data, and then recover the pose and scene geometry through minimizing the reprojection error based on these feature associations; and (ii) direct-based methods [11]–[13], that directly minimizes photometric errors in different event representations without explicit data association.

1) Feature-based Event Pose Tracking: The first featurebased event pose tracking method is proposed in Ref. [17] which fuses events with IMU through the Extended Kalman Filter. Subsequent to this, nonlinear optimization employing feature-based methods, EIO (event and IMU odometry) and EVIO (event, image, IMU odometry), were introduced in Ref. [18] and Ultimate-SLAM [14], where the image-like event frames were developed to leverage traditional imagebased feature detection and tracking. Ref. [19] introduces an EIO approach by addressing the reprojection error from the asynchronous events and directly incorporating IMU within a continuous-time framework. Ref. [20] combined the event-based and image-based feature tracker [21] as the front end with a filter-based back end. Ref. [22] presents a monocular feature-based EIO that employs event-corner features to provide real-time 6-DoF state estimation. Ref. [23] extracts features from events-only data and associates it with a spatio-temporal locality scheme based on exponential decay. Ref. [24] performs the event-only VO by optimizing the camera poses and 3D feature positions jointly. ES-VIO [16] proposed the first stereo EIO and EVIO framework to estimate states through temporally and spatially eventcorner feature association. IDOL [25] and Ref. [26], [27] explore the event-based line feature in state estimation. PL-EVIO [15] integrates event-based point and line features to perform robust pose estimations, which can be used as onboard pose feedback for the quadrotor to achieve aggressive flip motion.

2) Direct-based Event Pose Tracking: Ref. [28] presents an event-based direct method that leverages photometric relationships between brightness changes and absolute brightness intensity to associate events with the corresponding

pixels in the reference image. EVO [11] performs an eventbased tracking approach relying on edge-map (2D-3D) model alignment, utilizing the 3D map reconstructed from EMVS [2]. Ref. [29], [30] present direct-based tracking of an event camera from a given photometric depth map. ESVO [12] is the first stereo event-based VO method, which follows a parallel tracking and mapping scheme to estimate the ego motion through the 2D-3D edge registration on time surface (TS). Building upon the framework of ESVO, DEVO [31] introduces a direct VO framework that incorporates a depth camera to supply depth information for the event camera. EDS [13] proposed an event-image alignment algorithm that minimizes the photometric error between the brightness change from events and the image gradients, enabling 6-DOF pose tracking. However, most of the aforementioned direct-based event pose tracking methods are limited to small-scale environments and small, dedicated movements. They struggle to provide reliable state estimations, as they heavily depend on successful direct model alignment and the timely updates of the local 3D map. While the integration of both direct-based and feature-based methods in event-based pose tracking is still a research gap.

B. Event-based Mapping

1) Monocular Depth Estimation: Ref. [28] introduced the pioneering concept of purely event-based depth estimation by employing three decoupled probabilistic filters. EMVS [2] is the first work to achieve semi-dense 3D reconstruction from a single event camera with a known trajectory without requiring any explicit data association or intensity estimation. The concept of event-based denser mapping was introduced in Ref. [32], building upon EMVS [2]. However, it is still in the conceptual stage and does not successfully reconstruct any event-based dense point cloud. EOMVS [33] adopts omnidirectional event camera in EMVS [2] to reconstruct a wider field-of-view semi-dense map. Ref. [34] uses contrast maximization to find the best depth value that fits the event stream. These methods recover semi-dense 3D reconstructions of scenes by integrating events from a moving camera over a time interval, and they require knowledge of camera motion. Ref. [35] calculates semi-dense depth from optical flow using neuromorphic hardware to process asynchronous events. However, its applicability is confined to translational motion only. Besides, various learning-based methods have gained popularity in tackling the monocular event depth estimation problem, such as convolutional neural network (CNN) [5], [36], [37], recurrent neural networks (RNN) [38], and Neural Radiance Field (NeRF) [6], [39]-[41]. However, the exploration of non-learning approaches for a monocular event camera to recover dense and textured 3D structures remains an uncharted research area.

2) Stereo Depth Estimation: Ref. [42] follows a paradigm of event matching plus triangulation to realize the 3D reconstruction. Ref. [3] and ESVO [12] tackled a semidense reconstruction problem using a pair of temporally-synchronized event cameras in stereo configuration through energy minimization methods. T-ESVO [43] extends the

ESVO [12] using TSDF to reconstruct 3D environments and re-estimate the semi-dense depth. Refs. [4], [44] extend the EMVS [2] into stereo setup to estimate depth by fusing backprojected ray densities. Meanwhile, learning-based methods, such as Refs. [7]–[9], have been applied to stereo eventbased depth estimation, where different deep networks are developed to reconstruct event-based dense maps. Although these learning-based methods can predict dense depth and reveal 3D structures with limited events, they may struggle to handle objects that were not included in training sets, thus leading to uncertainties in their generalization ability. Furthermore, these learning-based methods can only generate localized depth maps. The production of globally consistent depth maps with rich texture information, such as surface mesh, remains an unexplored territory in the field of eventbased vision.

III. SYSTEM OVERVIEW

The proposed EVI-SAM utilizes inputs from a monocular event camera, including events, images, and IMU, to simultaneously estimate the 6 DoF pose and reconstruct the 3D dense maps of the environment. The overview of our EVI-SAM pipeline is illustrated in Fig. 2. Our EVI-SAM consists of tracking (Section IV) and mapping (Section V) modules, which operate in two parallel threads.

The tracking module employs a hybrid framework that combines feature-based and direct-based methods to process events, enabling the estimation of 6 DoF pose. A sliding windows graph-based optimization framework is designed to tightly fuse the event-based geometric error (re-projection residual) and event-based photometric error (relative pose residual), along with the image-based geometric error and the IMU pre-integration.

Concurrently, the mapping module initially reconstructs the event-based semi-dense depth using a space-sweep way through the 6 DoF pose obtained from the tracking module. Subsequently, it integrates an aligned intensity image as guidance to reconstruct the event-based dense depth and render the texture of the map (i.e., the color of 3D points). Finally, the TSDF-based map fusion is designed to generate a 3D global consistent texture map and surface mesh of the environment.

A. Event Representations

Event cameras are motion-activated sensors that capture pixel-wise intensity differences and report them as a continuous stream, rather than capturing the entire scene as an intensity image frame. An event can be triggered either by moving objects or the ego-motion of the camera and when a large enough intensity change exceeds the pre-defined threshold $T_{threshold}$, it can be represented as follows:

$$\boldsymbol{e} = \{t, u, v, p\} \Leftrightarrow \boldsymbol{I}(u, v, t + \triangle t) - \boldsymbol{I}(u, v, t) = p \cdot T_{threshold}$$
(1)

where t is the timestamp that the intensity of a pixel I(u,v) changes, and p is the polarity that indicates the direction of the intensity change. Since a single event lacks sufficient

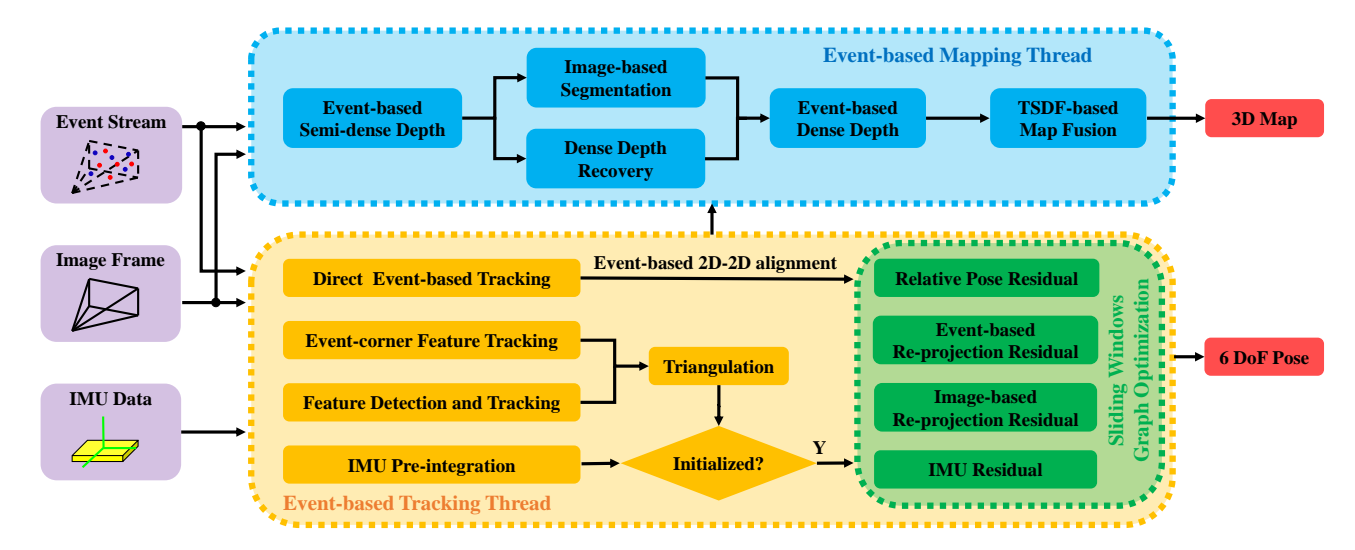


Fig. 2. System overview. The EVI-SAM algorithm takes events, images, and IMU as inputs, enabling the recovery of both camera pose and dense map of the scene. The mapping process takes raw event streams as input, using images for guidance, and produces dense and textured 3D mapping as output. The tracking thread takes event, image, and IMU as input, and constructs the feature-based and direct-based constraints to estimate the 6 DoF pose.

information, it is common to aggregate sets of events within time intervals into synchronous data representation, rather than processing individual events asynchronously. In the EVI-SAM, the mapping module takes the raw event streams as input, while the tracking module employs two distinct event representations (as shown in the left part of Fig. 1) as intermediate variables to facilitate the tracking between adjacent observations: the Time Surface (TS) with Polarity (Eq. (2)) for the event-corner feature tracking, and the event mat (Eq. (3)) for event-based 2D-2D alignment.

The TS with polarity can encode the spatio-temporal constraints of the historical event stream at any given instant. Using an exponential decay kernel, it can emphasize recent events compared to past events. Assuming t_{last} as the timestamp of the last event at each pixel coordinate $\boldsymbol{x}=(u,v)$, the TS with polarity at time $t \geq t_{last}(\boldsymbol{x})$ can be defined by:

$$T_p(\boldsymbol{x},t) = p \cdot \exp(-\frac{t - t_{last}(\boldsymbol{x})}{\eta})$$
 (2)

where η is the decay rate kernel.

The event mat is generated by aggregating a group of events that occur within a temporal neighborhood onto the event-accumulated image. In this process, pixel values are set to 255.0 when an event is triggered; otherwise, they are set to zero, as follows:

$$E_{t} = \sum_{t=t_{0}}^{t=t_{0}+\Delta t} \{e|t_{0} \le t \le t_{0} + \Delta t\}$$
 (3)

where Δt is the constant temporal window of the observed events.

IV. EVENT-BASED HYBRID POSE TRACKING

Our proposed event-based hybrid tracking module tightly integrates feature-based EVIO and event-based direct align-

ment within a graph-based nonlinear optimization framework. The feature-based EVIO (detailed in Section IV-C) consists of event-based landmarks, image-based landmarks, and IMU pre-integration. The event-based direct alignment (detailed in Section IV-B) takes continuous event streams as input and calculates the photometric error at the pixel level to establish relative pose constraints.

As for the feature-based EVIO (more details are available in [15], [22]), when a new event stream arrives, the first step is to track the existing event-corner features using optical flow on the TS with polarity denoted as $T_p(x,t)$ (see Eq. (2)). Any features that cannot be successfully tracked at the current timestamp are discarded. Subsequently, new event-corners are detected from the incoming event stream whenever the number of tracked features falls below a certain threshold. Meanwhile, the TS with polarity $T_p(x,t)$ is utilized as a mask to ensure the even distribution of event-corner features. After undistortion, outliers filtering, and triangulation, the event-based landmark, for which the 3D position has been successfully calculated, is integrated to establish the re-projection constraints.

Regarding the event-based direct alignment, direct refinement is performed on every event mat E_t by minimizing the photometric error to establish relative pose constraints. After that, a tightly joint optimization scheme (Eq. (4)) is performed over all the sliding windows which contains re-projection constraints and the relative pose constraints. To ensure the co-visibility between the feature-based and direct constraints, the state variables shared by these two constraints are synchronized before optimization.

A. Hybrid Optimization for Feature-based EVIO and Eventbased Direct Tracking

Events are more suitable for the direct methods compared to images, and they also inherently overcome challenges

associated with direct methods. Firstly, events are triggered by intensity change and naturally select high-gradient pixels, effectively substituting the gradient selection process in image-based direct methods [45]. Secondly, the high temporal resolution of events results in minimal displacement between two event frames, enabling the attainment of an optimal solution [46]. Thirdly, the event camera is immune to photometric distortions/variations, gradual brightness changes, and highly non-convex or non-linear intensity values. Besides, both feature-based and direct-based methods have their strengths and weaknesses in various aspects, which complement each other to some extent [47], [48]. The robustness provided by salient visual features makes feature-based methods well-suited for handling irregular scene variations and large inter-frame motions. Conversely, direct methods exhibit better resilience and superior accuracy in low-textured scenes by leveraging high-gradient sub-pixel alignment.

Therefore, we integrate the feature-based and direct-based methods into an event-based hybrid pose tracking, combining the superior robustness of feature-based event pose tracking and the relatively high accuracy achieved through event-based direct alignment. We define hybrid optimization as the process of maximizing a posterior based on feature-based and direct-based measurements. Assuming that these two measurements are independent of each other and the noise with each measurement is zero-mean Gaussian distributed. The hybrid optimization problem can be formulated as the minimization of a series of costs as follows:

$$\chi^* = \underset{\chi}{\operatorname{arg max}} p(\chi|z)$$

$$= \underset{\chi}{\operatorname{arg min}} \left\{ ||r_p - H_p \chi||^2 + \sum_{i=1}^n ||r(z_i, \chi)||_{P_i}^2 \right\}$$
(4)

where χ is the estimated state of the system, the state at the k^{th} timestamp is composed by the position $p_{b_k}^w$, and the orientation quaternion $q_{b_k}^w$, and the velocity $v_{b_k}^w$ of the IMU in the world frame $(\chi_k = [p_{b_k}^w, q_{b_k}^w, v_{b_k}^w])$. z stands for the aggregation of the independent feature-based and direct-based measurements (n=2) in our framework), and $\{r_p, H_p\}$ encapsulates the prior information or the marginalization of the system state. $r(\cdot)$ denotes the residual function of each measurement and $||\cdot||_P$ is the Mahalanobis norm. We decompose this optimization problem as two individual factors, the relative pose constraints from direct-based measurements (Eq. (6)), and the constraints from feature-based EVIO (Eq. (7)).

B. Event-based Direct Pose Tracking

The direct-based measurements of our framework align the observed 2D event mats of the two consecutive timestamps. The photometric error can be created by the 2D event mat E_t at two timestamps k and i:

$$e_{2D-2D} = \sum_{u,v} (\mathbf{E}_k - \mathbf{E}_i)$$

$$= \sum_{u,v} (\mathbf{E}(u_k, v_k) - \mathbf{E}(\Delta \mathbf{T}_i^k \mathbf{T}_e^b \pi_e^{-1}(u_i, v_i)))$$
(5)

where π_e^{-1} is the back-projection function of the event camera. T_e^b is the extrinsic matrix between the event camera frame and the body frame. While the data association of the pixel between these two event mats is completed using the inverse compositional Lucas-Kanade method (see Fig. 3(a)), which iteratively computes the incremental motion ΔT_i^k from the reference pose of the E_i at timestamp i to the current pose of the E_k at timestamp k.

Instead of directly incorporating the photometric error term in the graph optimization, the pose-pose constraint is leveraged to implicitly contain the relative transforms derived from the direct method. The relative pose constraint based on the optimized incremental pose ΔT_i^k in Eq. (5) is given by:

$$r(\boldsymbol{z}_{direct}, \boldsymbol{\chi}) = \sum_{i,k \in K} ||\Delta \boldsymbol{T}_i^k \cdot (\boldsymbol{T}_{b_i}^w)^{-1} \cdot \boldsymbol{T}_{b_k}^w||_{W_{direct}}^2 \quad (6)$$

where z_{direct} represents the direct-based measurements. K (K=10 in our experiments) is the number of keyframes in the sliding window. $T_{b_i}^w$ and $T_{b_k}^w$ are the pose of the body frame in the word frame in i^{th} and k^{th} keyframe. W_{direct}^k is the weight of the relative pose constraint.

An example of the event-based 2D-3D alignment is also illustrated in Fig. 3(b). Current event-based direct pose tracking methods [11]-[13], [31] reply on the 2D-3D geometric alignment, resulting in relatively lower localization accuracy and even failures in pose tracking. This could be attributed to the slow convergence of the estimated 3D map or the rapid changes in edge patterns between adjacent event packets. We posit that the effectiveness of the event-based 2D-3D alignment method relies heavily on the accurate construction of the event-based 3D depth map and its successful alignment with the current 2D event frame. This limitation results in a notable lack of robustness in these event-based direct pose tracking methods, particularly in scenarios involving aggressive motion or HDR. Conversely, our proposed eventbased 2D-2D alignment excels in performance without relying on the 3D depth maps, surpassing the performance of the conventional event-based 2D-3D alignment.

C. Feature-based EVIO Pose Tracking

The feature-based tracking module of our system is the same as the feature-based EVIO in our previous works [15], [22], where the camera poses are optimized by minimizing a joint nonlinear least-squares problem for the system state χ as follows:

$$r(\mathbf{z}_{feature}, \mathbf{\chi}) = \sum_{k=0}^{K-1} ||\mathbf{e}_{imu}^{k}||_{W_{imu}}^{2} + \sum_{k=0}^{K-1} \sum_{l \in \xi} ||\mathbf{e}_{image}^{k,l}||_{W_{image}}^{2} + \sum_{k=0}^{K-1} \sum_{l \in \zeta} ||\mathbf{e}_{event}^{k,l}||_{W_{event}}^{2}$$

$$(7)$$

Eq. (7) is composed of three components: (i) the IMU pre-integration residuals \boldsymbol{e}_{imu}^k with weight W_{imu}^k ; (ii) the feature-based image residual $\boldsymbol{e}_{image}^{k,l}$ with weight W_{image}^k ; (iii) the feature-based event residual $\boldsymbol{e}_{event}^{k,l}$ with weight

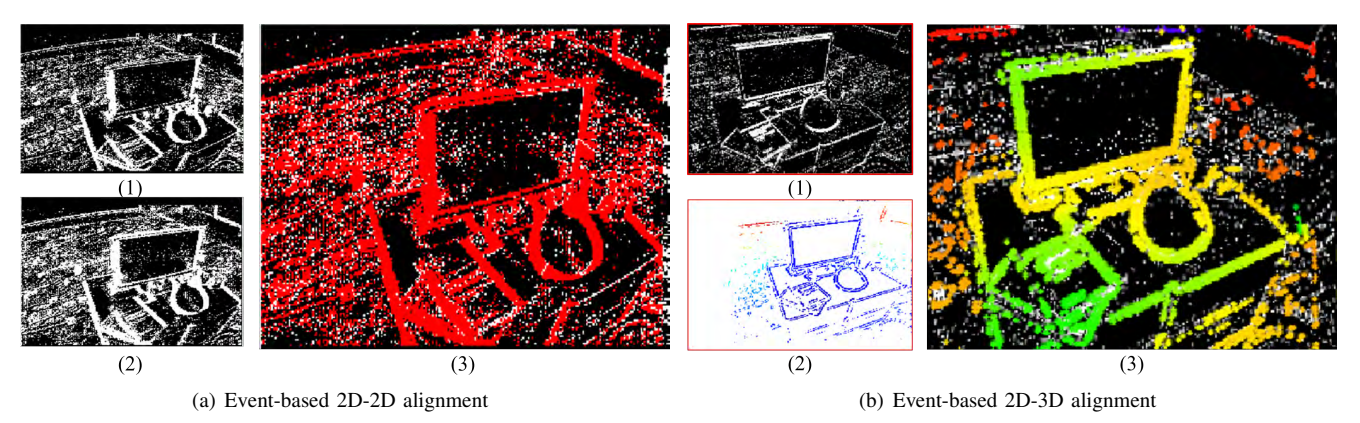


Fig. 3. Direct event-based alignment. (a) Event-based 2D-2D alignment: The 2D event mat in the current timestamp (a1) is warped to the 2D event mat in the previous timestamp (a2). The result (a3) is the alignment between the 2D current event mat (white) and the previous 2D event mat (red). (b) Event-based 2D-3D alignment: The current 2D event mat aggregated through a small number of events(b1) is warped to the projected mat recovered from the event-based 3D semi-dense depth in (b2). The result (b3) is a good alignment between the 2D current event mat (white) and the projected 3D event-based map (color).

 W^k_{event} . ζ and ξ are the set of event-corner features and image features, respectively. K (K=10 in our experiments) is the total number of keyframes in the sliding windows. The detailed mathematical explanation can be found in our previous work [15]. Here, we only review the re-projection constraint of the event-corner features. Considering the l^{th} event-corner feature that is first observed in the i^{th} keyframe, the residual for its observation in the k^{th} keyframe is defined as:

$$e_{event}^{k,l} = \begin{bmatrix} u_l^k \\ v_l^k \end{bmatrix} - \pi_e \cdot (\mathbf{T}_e^b)^{-1} \cdot \mathbf{T}_w^{b_k} \cdot \mathbf{T}_{b_i}^w \cdot \mathbf{T}_e^b \cdot \pi_e^{-1} (\frac{1}{\lambda_l}, \begin{bmatrix} u_l^i \\ v_l^i \end{bmatrix})$$
(8)

where λ_l is the inverse depth of the event-corner features; $[u_l^i, v_l^i]^{\rm T}$ is the first observation of the l^{th} event-corner feature in the i^{th} keyframe. $[u_l^k, v_l^k]^{\rm T}$ is the observation of the same event-corner feature in the k^{th} keyframe, π_e and π_e^{-1} denote the event camera projection and inverse projection like Eq. (6), respectively. $T_{b_i}^w$ indicates the movement of the body frame related to the world frame in timestamp i, $T_w^{b_k}$ is the transpose of the pose of the body in the world frame in the k^{th} keyframe.

V. EVENT-BASED DENSE MAPPING

The proposed event-based dense mapping module consists of three steps: (i) computing semi-dense depth map from event streams (Section V-A); (ii) reconstructing dense depth map from the event-based semi-dense depth with image as guidance (Section V-B); (iii) fusing the estimated local depth into global 3D map using TSDF-based fusion (Section V-C).

A. Purely Event-based Semi-dense Mapping

We developed the event-based space-sweep algorithm used in [2] to perform semi-dense depth estimation using a

monocular event camera, which targets a multi-view-stereo (MVS) problem. It consists of two steps: building a disparity space image (DSI) using a space sweeping method [49] from different reference viewpoints (RV), and then identifying the local maxima of the DSI to determine the depth value of the pixel.

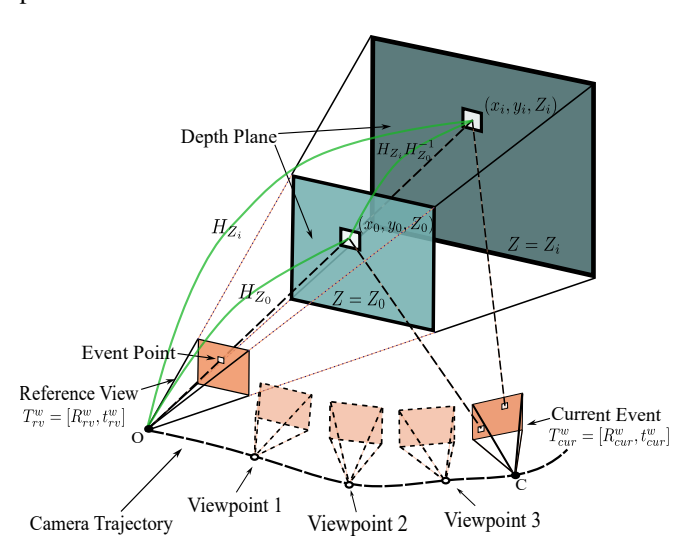


Fig. 4. The model of event-based back-projection and space sweeping calculations across different depth planes of the DSI.

A new RV would be chosen when the motion of the event camera surpasses a specified threshold. Subsequently, all events occurring between two consecutive RVs are backprojected to the front RV. The creation of an RV triggers the construction of an associated local depth map from that viewpoint. The back-projection rays from these nearby viewpoints are the perspective projection rays of 2D events into the 3D space (DSI) based on the camera model. The DSI, shown in Figs. 4 and 6(b), is a 3D voxel grid constructed for each RV. It describes the distribution of event back-projected

rays and the scores stored in each voxel (i.e., the number of back-projected rays passing through each voxel from nearby viewpoints). The DSI is defined by N depth planes $\{Z_i\}_{i=1}^{N-1}$ and discretizing each depth plane into $w \times h \times N$ cuboid voxels, where w and h are the width and height of the event camera, respectively. N is equal to 100 in our implementation. The back-projecting events to the DSI can be discretized to the execution of mapping events to all the depth planes. Warping the points (u_i, v_i) from the current event camera to the canonical plane $Z = Z_0$ of RV using the planar homography $\mathbf{H}_{Z_0}(u_i, v_i, 1)^{\mathrm{T}} \to (x(Z_0), y(Z_0), 1)^{\mathrm{T}}$:

$$\boldsymbol{H}_{Z_0}^{-1} = \boldsymbol{R}_{rv}^{cur} + \frac{1}{Z_0} \boldsymbol{t}_{rv}^{cur} \boldsymbol{e}_3^{\mathrm{T}}$$
 (9)

where $e_3 = (0, 0, 1)^T$; \mathbf{R}_{rv}^{cur} and \mathbf{t}_{rv}^{cur} is the rotation matrix, translation vector from the RV to the current event camera:

$$\boldsymbol{T}_{rv}^{cur} = \begin{bmatrix} \boldsymbol{R}_{rv}^{cur} \\ \boldsymbol{t}_{rv}^{cur} \end{bmatrix} = (\boldsymbol{T}_{w}^{rv} \cdot \boldsymbol{T}_{cur}^{w})^{-1} = ((\boldsymbol{T}_{rv}^{w})^{-1} \cdot \boldsymbol{T}_{cur}^{w})^{-1}$$
(10)

where T_{cur}^w and T_{rv}^w are the pose of the event camera in the current timestamp and the pose of the RV related to the world frame from the tracking module of EVI-SAM, respectively. After that, the events in the other plane of DSI are transformed with the depth from $Z = Z_0$ to $Z = Z_i$ (shown in Fig. 4) using the following equation:

$$\boldsymbol{H}_{Z_{i}}\boldsymbol{H}_{Z_{0}}^{-1} = \left(\boldsymbol{R}_{rv}^{cur} + \frac{1}{Z_{i}}\boldsymbol{t}_{rv}^{cur}\boldsymbol{e}_{3}^{\mathrm{T}}\right)^{-1} \left(\boldsymbol{R}_{rv}^{cur} + \frac{1}{Z_{0}}\boldsymbol{t}_{rv}^{cur}\boldsymbol{e}_{3}^{\mathrm{T}}\right)$$
(11)

The optical center of the event camera in the coordinate frame of the RV can be defined as:

$$\boldsymbol{X} = (X_c, Y_c, Z_c) = -(\boldsymbol{R}_{rv}^{cur})^{\mathrm{T}} * \boldsymbol{t}_{rv}^{cur}$$
(12)

Then, we can calculate the transformation of points (u_i, v_i) in the canonical plane $Z = Z_i$, the $(x(Z_i), y(Z_i))$ as follows:

$$x(Z_{i}) = \frac{Z_{0}(Z_{i} - Z_{0})}{Z_{i}(Z_{0} - Z_{c})}x(Z_{0}) + \frac{1}{Z_{i}}(1 - \frac{(Z_{i} - Z_{0})}{(Z_{0} - Z_{c})})X_{c}$$

$$y(Z_{i}) = \frac{Z_{0}(Z_{i} - Z_{0})}{Z_{i}(Z_{0} - Z_{c})}y(Z_{0}) + \frac{1}{Z_{i}}(1 - \frac{(Z_{i} - Z_{0})}{(Z_{0} - Z_{c})})Y_{c}$$
(13)

After back-projecting events to DSI, we count the number of back-projection rays that pass through each voxel and determine whether or not a 3D point exists in each voxel. Based on the theory that the regions where multiple back-projection rays nearly intersect are likely to be a 3D point in the scene, the 3D points can be determined when the scores of the DSI voxels are at a local maximum. The culmination of all these 3D points onto the image plane constitutes the semi-dense depth.

B. Image-guided Event-based Dense Mapping

Events are sparse and mostly respond to moving edges so the event-based semi-dense depth is also incomplete, only capturing depths at edges. Inspired by Ref. [50], it is possible to reconstruct the geometry of an unknown environment using sparse and incomplete depth measurements. Therefore, in this section, we leverage the complementary strengths of event-based and standard frame-based cameras by incorporating additional intensity images as guidance for event-based dense depth completion. It builds on the theories that depth discontinuities are commonly correlated with intensity boundaries, whereas homogeneous intensity regions correspond to homogeneous depth parts [51]. Moreover, pixels sharing the same intensity values are likely to belong to the same block in the depth image [52].

To this end, we can interpolate or fill the hole of the event-based semi-dense map based on the surrounding sparse depth information and the edges extracted from intensity images. We first select the intensity image captured at the RV (Fig. 6(g)) to ensure proper alignment with the event-based semi-dense depth. Next, we employ the region-growing approach to segment the image, as depicted in Fig. 6(h). Other different segmentation or edge extraction operators could also be used, though satisfactory results have already been obtained using such simple selection. After that, all the semi-dense depth points at the current RV are projected onto the segmentation regions. Since events are only generated at pixels where brightness changes occur, they naturally align with contours. Finally, the vacant depth region can be filled or inpainted by using the weighted sum of the depthrecovered projected event points within the corresponding segmentation region.

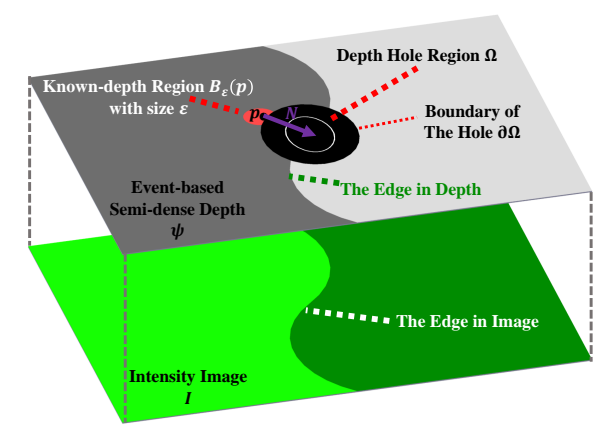


Fig. 5. The model of our event-based dense mapping incorporates edges derived from the intensity image as guidance. The upper layer represents the event-based semi-dense depth. This layer includes areas where the depth is known (regions successfully recovered through semi-dense mapping, marked in red) and areas with unknown depth (marked in black). The lower layer represents the intensity image with boundary information after segmentation. Since events are triggered in regions with edges, the semi-dense depth and the intensity image edges at the corresponding locations are consistent.

We extend the fast marching method [53] to incorporate the intensity image as guidance during the filling or inpainting process for holes in the event-based semi-dense depth, ultimately producing the event-based dense depth. We firstly estimate the depth of a pixel located on the boundary of unknown regions, as illustrated in Fig. 5, in which the depth

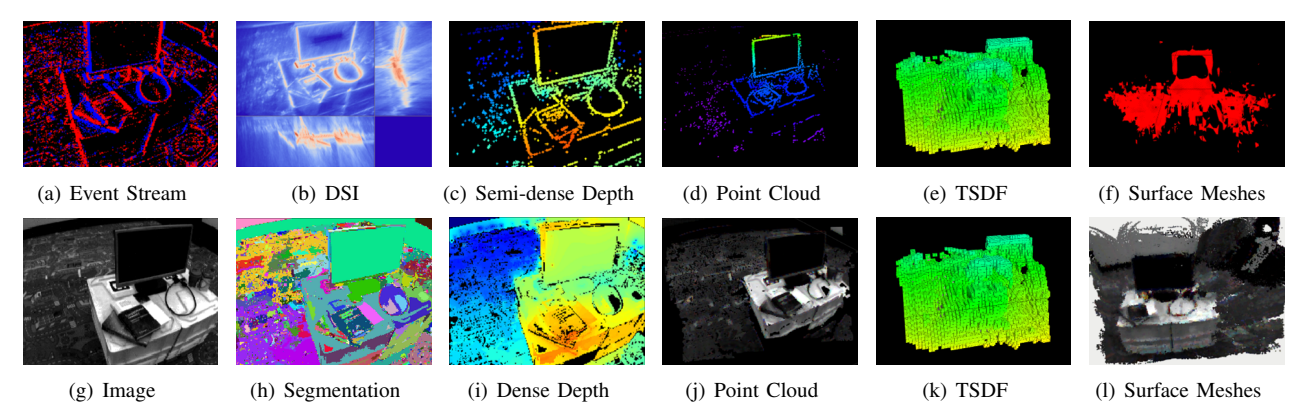


Fig. 6. The event-based semi-dense and dense mapping of our EVI-SAM. (a) The raw event stream and (g) the intensity image from the event camera; (b) The disparity space image (DSI) of the reference view (RV) point; (c) The purely event-based semi-dense depth generated from our EVI-SAM; (d) The point cloud of the event-based semi-dense depth; (e) The occupied node of the semi-dense mapping after TSDF-fusion; (f) The surface mesh of the semi-dense mapping; (h) The segmentation on the image; (i) The event-based dense depth generated from our EVI-SAM; (j) The point cloud of the event-based dense depth with texture information; (k) The occupied node of the dense mapping after TSDF-fusion; (l) The surface mesh of the dense mapping;

value of point p is unknown situated on the boundary $\partial\Omega$ of the depth-hole region Ω in the event-based semi-dense depth ψ . Considering a small neighborhood region $B_{\varepsilon}(p)$ with size ε , where the depth values are known around point p in the semi-dense depth ψ . Assuming the depth values have similarities in the local region, the inpainting value of p should be determined by the values of the known-depth region near p. If ε is small enough, we can consider the first order approximation $d(p,q), q \in B_{\varepsilon}(p)$, the contribution value of point q to p can be denoted as:

$$d(\mathbf{p}, \mathbf{q}) = d(\mathbf{q}) + \nabla d(\mathbf{q})(\mathbf{p} - \mathbf{q}) \approx d(\mathbf{q})$$
(14)

where d(q) is the depth value of point q, and $\nabla d(q)$ indicates the depth gradient at the pixel q.

Next, the filled value of point p can be calculated by the weighted sum of all the contribution values of points q in the $B_{\varepsilon}(p)$, as follows:

$$d(\mathbf{p}) = d(\mathbf{p}, \omega) = \frac{\sum_{\mathbf{q} \in \mathbf{B}_{\varepsilon}(\mathbf{p})} \omega_{\mathbf{p}, \mathbf{q}} d(\mathbf{p}, \mathbf{q})}{\sum_{\mathbf{q} \in \mathbf{B}_{\varepsilon}(\mathbf{p})} \omega_{\mathbf{p}, \mathbf{q}}}$$

$$= \frac{\sum_{\mathbf{q} \in \mathbf{B}_{\varepsilon}(\mathbf{p})} \omega_{\mathbf{p}, \mathbf{q}} d(\mathbf{q})}{\sum_{\mathbf{q} \in \mathbf{B}_{\varepsilon}(\mathbf{p})} \omega_{\mathbf{p}, \mathbf{q}}}$$
(15)

$$\omega_{\mathbf{p},\mathbf{q}} = |\omega_{dir} \cdot \omega_{dst} \cdot \omega_{lev} \cdot \omega_{img}| \tag{16}$$

where $\omega_{p,q}$ is the weighting coefficient that measures the similarity of depth value between the point p and q.

The term of ω_{dir} ensures that pixels closer to the normal direction N(p) have higher contributions, defined as follows:

$$\omega_{dir} = \frac{p - q}{||p - q||} \cdot N(p) \tag{17}$$

The weight ω_{dst} in Eq. (16) determines the contribution of pixels based on geometric distances to p.

$$\omega_{dst} = \frac{1}{||\boldsymbol{p} - \boldsymbol{q}||^2} \tag{18}$$

This term is directly associated with the continuity of depth, and we have empirically observed that its contribution is larger than that of other terms.

The term of ω_{lev} in Eq. (16) represents the level set term, assigning a higher weight to pixels closer to the contour through p, as follows:

$$\omega_{lev} = \frac{1}{1 + |T(\boldsymbol{p}) - T(\boldsymbol{q})|} \tag{19}$$

where T(p) is the distance of point p to the initial boundary of depth-hole. $\nabla T(p) = N(p)$ denotes the normal of hole boundary at the point p. The missing data is repaired pixel-wisely and the pixel with smaller T(p) has a higher inpainting priority.

Lastly, the weight ω_{img} in Eq. (16) ensures that pixels with similar pixel intensity to I(p) contribute more than others:

$$\omega_{img} = e^{-\frac{||I(p)-I(q)||^2}{2}}$$
 (20)

I(p) and I(q) indicates the intensity value of the image at point p and q. This term allows the weighting function in Eq. (16) to integrate intensity information for dense depth recovery. Pixels with similar intensity values are more likely to be part of the same block in the depth image, resulting in a higher weight.

To fill the whole region Ω and generate the event-based dense depth, after recovering the depth of pixels on the boundary $\partial \Omega$ of the depth hole Ω , we propagate the depth from $\partial \Omega$ to Ω through iteratively applying Eq. (15). Firstly, we set T(p)=0 for pixels in known regions and progressively generate the distance map T(p) while marching into Ω , ensuring $||\nabla T(p)||=1$. To remove the outliers and preserve the sharpness of depth discontinuities, we employ the bilateral and non-local means filter on the event-based dense depth (Fig. 6(i)). Finally, we render the texture information from the intensity image onto the event-based 3D point cloud to obtain a textured map (Fig. 6(j)).

C. TSDF-based Map Fusion

Since the depth estimation from a moving event camera contains noticeable outliers, this motivates us to explicitly model the inliers probability of each estimated depth and take outliers into account in the depth fusion step. The TSDF can rapidly build and alleviate sensor noise across numerous observations, and it can also be further designed to generate surface meshes. Therefore, instead of simply stitching all local depth maps into the global map, we introduce the TSDF-based approach [54] to describe the 3D representation of environments and fuse the local depth into global and long-term historical depth.

TSDF can construct the global environmental surface representation based on consecutive depth maps and associated camera poses. To merge the event-based local depth into a TSDF, we perform the ray-cast from the origin of the event camera to each depth point in the event-based local depth map. Meanwhile, we update the signed distance and weight values of TSDF voxels along this ray. The merging of local depths is based on the current distance D_{last} and the weight value W_{last} of a TSDF voxel, as well as the new update values from a specific point observation in the event-based local depth map.

Given a center position of TSDF voxel ($V \in \mathbb{R}^3$) is passed by a ray between a 3D depth point ($P \in \mathbb{R}^3$), and the event camera origin ($O \in \mathbb{R}^3$). The updated TSDF distance value D_{new} and the weight value W_{new} for this voxel described as follows:

$$D_{new} = \frac{W_{last} \cdot D_{last} + wd}{W_{last} + w},$$

$$W_{new} = min(W_{last} + w, W_{max}),$$
(21)

where d is the distance from the TSDF voxel center V to the new coming 3D depth point P, defined as follows:

$$d = \|\mathbf{P} - \mathbf{V}\|sign[(\mathbf{P} - \mathbf{V}) \cdot (\mathbf{P} - \mathbf{O})]$$
 (22)

While for the weight w of this new coming 3D depth point, we follow Ref. [55] to define it with the behind-surface dropoff as:

$$w = \begin{cases} \frac{1}{\rho^2}, & -\varepsilon \le d\\ \frac{1}{\rho^2} \cdot \frac{1}{d_t - \varepsilon} (d + d_t), & -d_t \le d < -\varepsilon\\ 0, & d < -d_t \end{cases}$$
 (23)

where ρ is the depth value of the event-based local depth in the event frame; $d_t=4\varepsilon$ is the truncated distance for TSDF, and ε represents the size of voxel ($\varepsilon=0.01$ in our implementation).

Following the creation and update of TSDF voxels, the global depth map will be refined based on Eq. (21). For each depth point in the event-based local depth maps, we project its position onto the TSDF voxel grid, and group it with all other depth points mapping to this voxel. Subsequently, we compute the weighted mean of all points within each TSDF voxel and perform raycasting only once on this mean position. The surface meshes can also be reconstructed from updated TSDF voxels (shown in Figs. 6(f) and 6(l)), which allow us to get a better assessment of the perception environment.

VI. EVALUATION

This section comprehensively evaluates the performance of our EVI-SAM system in terms of pose tracking and 3D mapping, employing both quantitative and qualitative assessments through extensive experiments.

Firstly, we show the effectiveness of our event-based hybrid pose tracking module by comparing the estimated trajectories against the ground truth pose in challenging situations (Section VI-A).

Secondly, we assess the mapping performance of EVI-SAM through four sets of experiments. The first set (Section VI-B) evaluates the mapping performance across diverse scenarios to show the generation ability of our event-based dense mapping method. Section VI-C compares our 3D mapping approach with other 3D reconstruction baselines. Moreover, Section VI-D evaluates our mapping performance under challenging situations, such as HDR (Section VI-D1), and the scenarios involving aggressive motion (Section VI-D2). Section VI-E evaluates the overall system on the onboard platform, including comparing local mapping with a commercial depth camera and assessing the global event-based 3D dense reconstruction performance.

Finally, the analysis of the computational performance and the discussion of the limitations are completed in Section VI-F and Section VI-G, respectively.

A. Tracking Performance in Aggressive Motion and HDR Scenarios

To evaluate the tracking performance of our event-based hybrid framework in challenging scenarios, we compare our system with other state-of-the-art image-based or event-based VO/VIO using publicly available datasets: DAVIS240c [56], HKU-dataset¹ and VECtor [62]. These datasets offer events, grayscale frames, IMU, and ground truth poses. The criterion used to assess tracking accuracy is the mean absolute trajectory error, which aligns the estimated trajectory with the ground-truth pose in the 6-DOF transformation (SE3).

Table I and Table II report the results on these benchmarks, encompassing challenge scenarios such as HDR, aggressive motion, large-scale, as well as textureless environments. The best results for each sequence are highlighted in bold. In Table I, we directly report raw results from the original papers we compared, since the same trajectory alignment protocol is utilized. Our EVI-SAM achieves the best performance among event-based VIO with slight improvement compared to PL-EVIO. This highlights the effectiveness of our hybrid pose tracking pipeline, with the improvement stemming from the proposed event-based 2D-2D alignment. Table II demonstrates that our proposed hybrid tracking pipeline effectively combines the robustness of the feature-based method with the high accuracy achieved by the direct-based method. Compared to pure direct eventbased VO methods (e.g., EVO [11], ESVO [12]) or pure feature-based EVIO methods (e.g., Ultimate SLAM [14]),

¹https://github.com/arclab-hku/Event_based_VO-VIO-SLAM

TABLE I. Accuracy Comparison of Our EVI-SAM with Other EIO/EVIO Works in DAVIS240c Dataset [56]

Cannanaa	Ref. [17]	Ref. [18]	Ref. [14]	Ref. [14]	Ref. [57]	Ref. [20]	Ref. [58]	EIO [22]	PL-EVIO [15]	Ref. [59]	Our EVI-SAM
Sequence	(E+I)	(E+I)	(E+I)	(E+F+I)	(E+I)	(E+F+I)	(E+I)	(E+I)	(E+F+I)	(E+F+I)	(E+F+I)
boxes_translation	2.69	0.57	0.76	0.27	2.55	0.48	1.0	0.34	0.06	0.74	0.11
hdr_boxes	1.23	0.92	0.67	0.37	1.75	0.46	1.8	0.40	0.10	0.69	0.13
boxes_6dof	3.61	0.69	0.44	0.30	2.03	0.84	1.5	0.61	0.21	0.77	0.16
dynamic_translation	1.90	0.47	0.59	0.18	1.32	0.40	0.9	0.26	0.24	0.71	0.30
dynamic_6dof	4.07	0.54	0.38	0.19	0.52	0.79	1.5	0.43	0.48	0.86	0.27
poster_translation	0.94	0.89	0.15	0.12	1.34	0.35	1.9	0.40	0.54	0.28	0.34
hdr_poster	2.63	0.59	0.49	0.31	0.57	0.65	2.8	0.40	0.12	0.52	0.15
poster_6dof	3.56	0.82	0.30	0.28	1.50	0.35	1.2	0.26	0.14	0.59	0.24
Average	2.58	0.69	0.47	0.25	1.45	0.54	1.56	0.39	0.24	0.65	0.21

Unit:%, 0.21 means the average error would be 0.21m for 100m motion; Aligning 5 seconds [0-5s] of the estimated trajectory with the ground truth; The notations E, F, and I stand for the use of event, frame, and IMU, respectively.

TABLE II. Accuracy Comparison of Our EVI-SAM with Other Image-based or Event-based Methods

		ORB-SLAM3 [60] (F+F+I)	VINS-Fusion [61] (F+F+I)	EVO [11]	ESVO [12] (E+E)	Ultimate SLAM [14] (E+F+I)	PL-EVIO [15] (E+F+I)	Our EVI-SAM (E+F+I)
Sequence		MPE / MRE	MPE / MRE	(E)	MPE / MRE	MPE / MRE	MPE / MRE	MPE / MRE
	hku agg translation	0.15 / 0.075	0.11 / 0.019	failed	failed	0.59 / 0.020	0.07 / 0.091	0.17 / 0.056
HKU dataset	hku agg rotation	0.35 / 0.11	1.34 / 0.024	failed	failed	3.14 / 0.026	0.23 / 0.12	0.24 / 0.056
	hku agg flip	0.36 / 0.39	1.16 / 2.02	failed	failed	6.86 / 2.04	0.39 / 2.23	0.32 / 2.08
	hku_agg_walk	failed	failed	failed	failed	2.00 / 0.16	0.42 / 0.14	0.26 / 0.22
	hku hdr circle	0.17 / 0.12	5.03 / 0.60	failed	failed	1.32 / 0.54	0.14 / 0.62	0.13 / 0.56
	hku_hdr_slow	0.16 / 0.058	0.13 / 0.026	failed	failed	2.80 / 0.099	0.13 / 0.068	0.11 / 0.033
	hku_hdr_tran_rota	0.30 / 0.042	0.11 / 0.021	failed	failed	2.64 / 0.13	0.10 / 0.064	0.11 / 0.026
	hku hdr agg	0.29 / 0.085	1.21 / 0.27	failed	failed	2.47 / 0.27	0.14 / 0.30	0.10 / 0.26
	hku_dark_normal	failed	0.86 / 0.028	failed	failed	2.17 / 0.031	1.35 / 0.081	0.85 / 0.052
	corner-slow	1.49 / 14.28	1.61 / 14.06	4.33 / 15.52	4.83 / 20.98	4.83 / 14.42	2.10 / 14.21	2.50 / 14.82
	robot-normal	0.73 / 1.18	0.58 / 1.18	3.25 / 2.00	failed	1.18 / 1.11	0.68 / 1.25	0.67 / 0.85
	robot-fast	0.71 / 0.70	failed	failed	failed	1.65 / 0.56	0.17 / 0.74	0.22 / 0.41
	desk-normal	0.46 / 0.41	0.47 / 0.36	failed	failed	2.24 / 0.56	3.66 / 0.45	1.45 / 0.28
	desk-fast	0.31 / 0.41	0.32 / 0.33	failed	failed	1.08 / 0.38	0.14 / 0.48	0.18 / 0.38
	sofa-normal	0.15 / 0.41	0.13 / 0.40	failed	1.77 / 0.60	5.74 / 0.39	0.19 / 0.46	0.19 / 0.20
VECtor [62]	sofa-fast	0.21 / 0.43	0.57 / 0.34	failed	failed	2.54 / 0.36	0.17 / 0.47	0.98 / 0.31
	mountain-normal	0.35 / 1.00	4.05 / 1.05	failed	failed	3.64 / 1.06	4.32 / 0.76	1.39 / 0.65
	mountain-fast	2.11 / 0.64	failed	failed	failed	4.13 / 0.62	0.13 / 0.56	0.38 / 0.30
	hdr-normal	0.64 / 1.20	1.27 / 1.10	failed	failed	5.69 / 1.65	4.02 / 1.52	5.74 / 0.87
	hdr-fast	0.22 / 0.45	0.30 / 0.34	failed	failed	2.61 / 0.34	0.20 / 0.50	0.67 / 0.26
	corridors-dolly	1.03 / 1.37	1.88 / 1.37	failed	failed	failed	1.58 / 1.37	1.58 / 1.38
	corridors-walk	1.32 / 1.31	0.50 / 1.31	failed	failed	failed	0.92 / 1.31	1.27 / 1.35
	school-dolly	0.73 / 1.02	1.42 / 1.06	failed	10.87 / 1.08	failed	2.47 / 0.97	1.53 / 0.89
	school-scooter	0.70 / 0.49	0.52 / 0.61	failed	9.21 / 0.63	6.40 / 0.61	1.30 / 0.54	1.46 / 0.53
	units-dolly	7.64 / 0.41	4.39 / 0.42	failed	failed	failed	5.84 / 0.44	0.59 / 0.35
	units-scooter	6.22 / 0.22	4.92 / 0.24	failed	failed	failed	5.00 / 0.42	0.83 / 0.38

Unit: MPE(%) / MRE(deg/m); Aligning the whole ground truth trajectory with estimated poses; The notations E, F, and I stand for the use of event, frame, and IMU, respectively.

our EVI-SAM significantly surpasses them in both accuracy and robustness. While compared with PL-EVIO [15], a feature-based method, our EVI-SAM also outperforms it in most sequences.

An interesting phenomenon regarding the pure direct-based methods, the EVO [11] and ESVO [12], is that both of them crashed in most of the sequences listed in Table II, with only a few sequences complete. However, even in cases where they are completed successfully, these methods exhibit significant errors when compared to the ground truth poses. This can be attributed to the challenges presented by these evaluation sequences, especially those containing aggressive motion. Consequently, approaches relying on edge-map (2D-3D) model alignment struggle to provide reliable state estimations, as they heavily depend on the timely updates of the local 3D map. Our proposed event-

based 2D-2D alignment method does not suffer from these shortcomings. Our event-based hybrid tracking module is robust and accurate enough to handle state estimation in such challenging situations.

We further analyze the performance comparison between feature-based and direct-based EVIO. To ensure a fair comparison, we individually run the direct-based event tracking pipeline of EVI-SAM (Direct-based), the feature-based event tracking pipeline of EVI-SAM (Feature-based), and the entire EVI-SAM system (includes both the direct-based and feature-based pipelines, marks as F-D-based). We visualize the estimated results for translation along the X-Y-Z axes and rotation around the roll-pitch-yaw axes, along with the ground truth in Fig. 7(a) and 7(b). It is evident that the introduction of our event-based 2D-2D alignment significantly enhances the performance of pose tracking. For instance, in

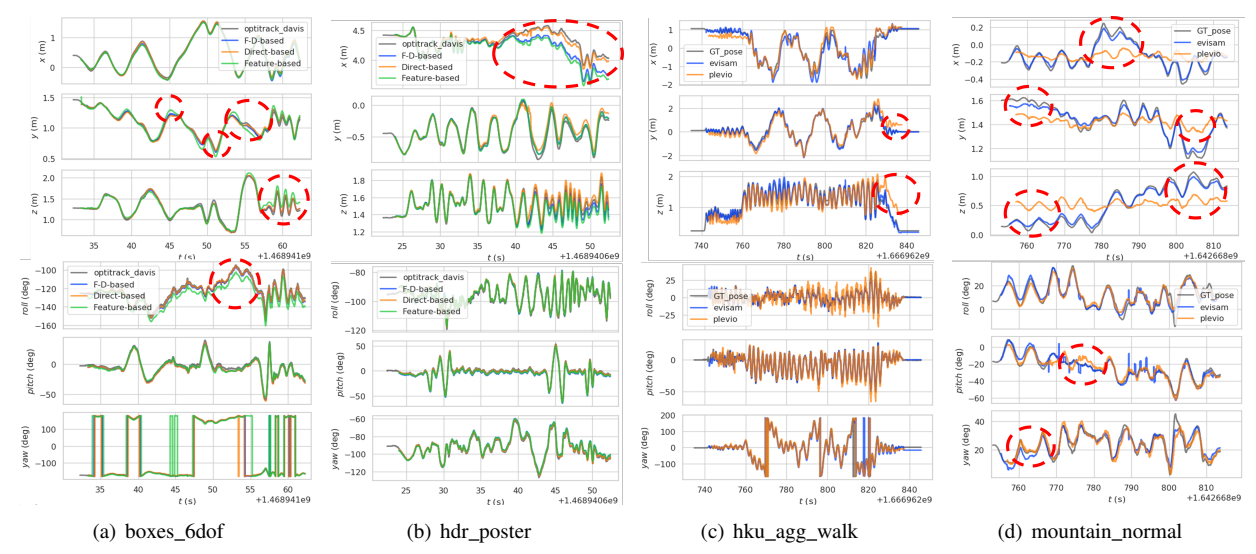


Fig. 7. Comparing the estimated trajectory in terms of translation and rotation produced by our EVI-SAM with the ground truth trajectory in DAVIS240C [56], HKU-dataset, and VECtor [62]. (a) and (b) show the comparison among our EVI-SAM with a feature-based event pipeline only, a direct-based event pipeline only, and the full event-based hybrid pipeline (feature-based + direct-based, F-D-based); (c) and (d) show the comparison between the PL-EVIO (feature-based) and our EVI-SAM (hybrid). The red dashed lines highlight the disparity between featured-based and direct-based methods.

the X-axes of Fig. 7(b), the Feature-based method deviates significantly from the ground truth between the 45th to 50th seconds, whereas the Direct-based method attains higher accuracy during this interval. Regarding the F-D-based, it has some offset influenced by the feature-based pipeline, but its performance remains superior to that of the standalone feature-based event tracking pipeline. On the other hand, it proves effective in handling irregular scene variations and large inter-frame motions, as evidenced by Table II. Our entire EVI-SAM system not only improves the accuracy compared to the standalone feature-based event tracking pipeline but also retains the advantages of the feature-based method.

Furthermore, we use PL-EVIO as a representative of the feature-based method and compare its 6-DoF estimation results with those of our EVI-SAM, as illustrated in Figs. 7(c) and 7(d). It is worth noting that although the numerical improvement in accuracy may not be pronounced in the tables due to statistical considerations, the effectiveness of our hybrid approach over a pure feature-based method is more evident when examining Fig. 7, particularly in local state estimation. This validates the improvement in event-based pose tracking and highlights the significance of introducing our event-based 2D-2D direct alignment method, particularly in conjunction with the feature-based method.

B. Mapping Performance in Diverse Scenarios

In this section, we evaluate the mapping performance of our EVI-SAM across diverse platforms and scenarios, including handle-held devices (such as rpg [3], DAVIS240C [56], HKU-dataset, VECtor [62]), flying drones (MVSEC [63]), and driving vehicles (DSEC [64]). These datasets provide event streams, grayscale frames, and IMU

data. The event stream has a resolution of 240×180 pixels for rpg [3] and DAVIS240C [56], 346×260 pixels for DAVIS346 in MVSEC [63] and HKU-dataset, 640×480 pixels for VECtor [62] and DSEC [64]. Additionally, These datasets span a wide range of scenarios, from indoor to outdoor autonomous driving, featuring scenes with varying texture richness, ranging from well-lit to dimly lit conditions, and encompassing both dynamic and static objects. We evaluate the full EVI-SAM system utilizing the event-based hybrid tracking module to provide pose feedback and demonstrate the generalization capability of our event-based dense mapping.

As some sequences lack ground truth depth, we only present qualitative mapping results in Fig. 8. The mapping results evident that our method does a notable job of reconstructing 3D dense structures with texture information, despite encountering such diverse scenarios, thus demonstrating its excellence and generalization ability in realworld scenes. Unlike the event-based dense mapping using learning approaches that require scene-specific pre-training, our proposed event-based dense mapping effectively recovers dense depth and texture information across diverse scenes. While these learning-based methods typically require specific pre-training for various scenes, resulting in limited generalization capabilities. This highlights the robustness and powerful generalization capability of our algorithm, distinguishing it from learning-based approaches [7], [9], [10], [41] that typically assess only a limited number of sequences within the same scene. Additionally, as evident in Figs. 8(o) - 8(t), the geometry of 3D scenes and the textures of buildings or vehicles have been effectively reconstructed. Notably, in Fig. 8(s), the reconstruction of the crosswalk on the road is particularly well-executed. In the dense depth, the black areas indicate instances where depth recovery was

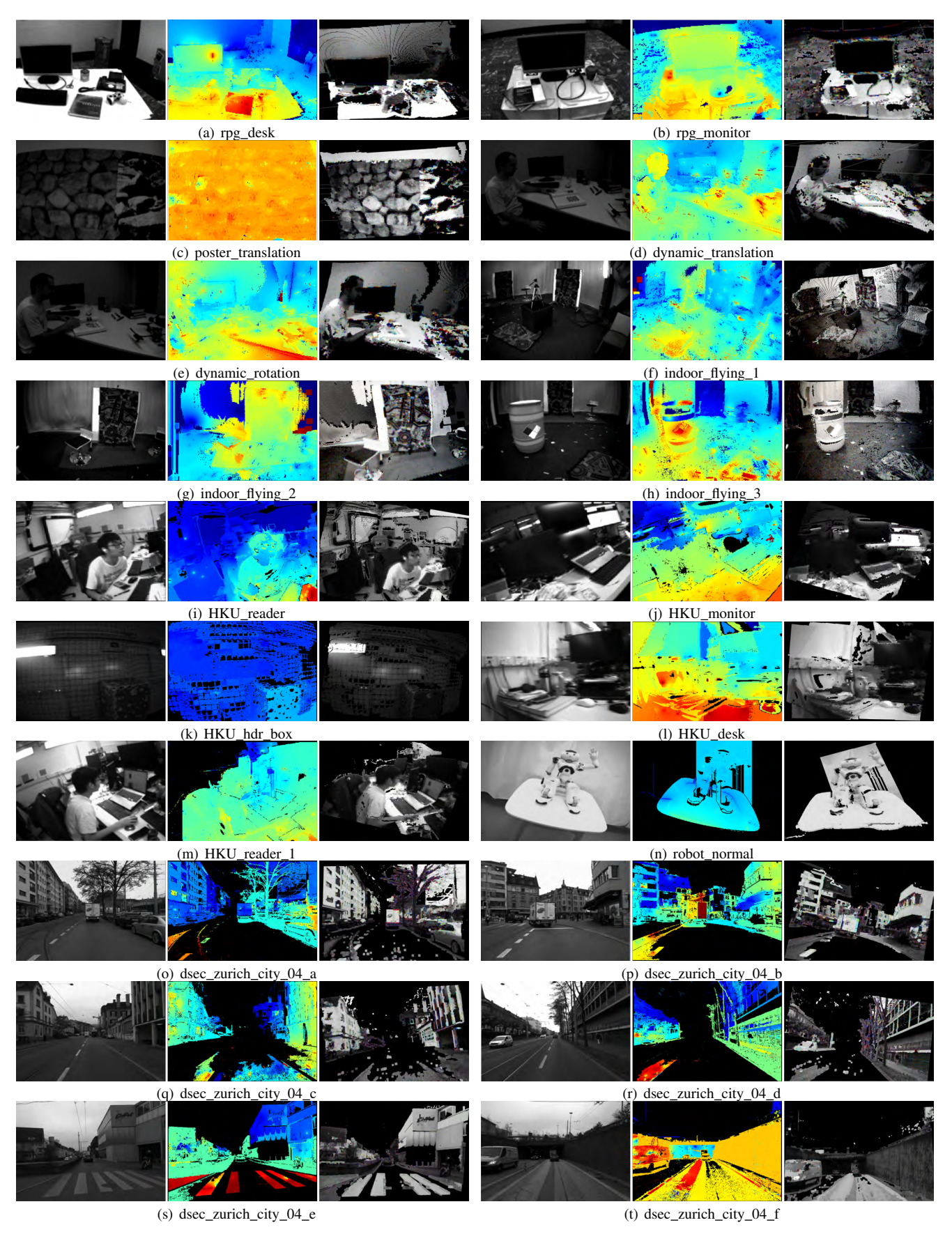


Fig. 8. Qualitative mapping result of our EVI-SAM in various data sequences. Each element includes the image view, dense depth, and the point cloud with texture information. The depth is pseudo-colored, from red (close) to blue (far), in the range of 0.55-6.25 m for the rpg [3] and davis240c [56]; in the range 1.0-6.5 m for MVSEC [63]; in the range 0.5-4.0 m for HKU-dataset; in the range 0.3-3.0 m for VECtor [62]; in the range 4.0-200 m for DSEC [64], respectively.

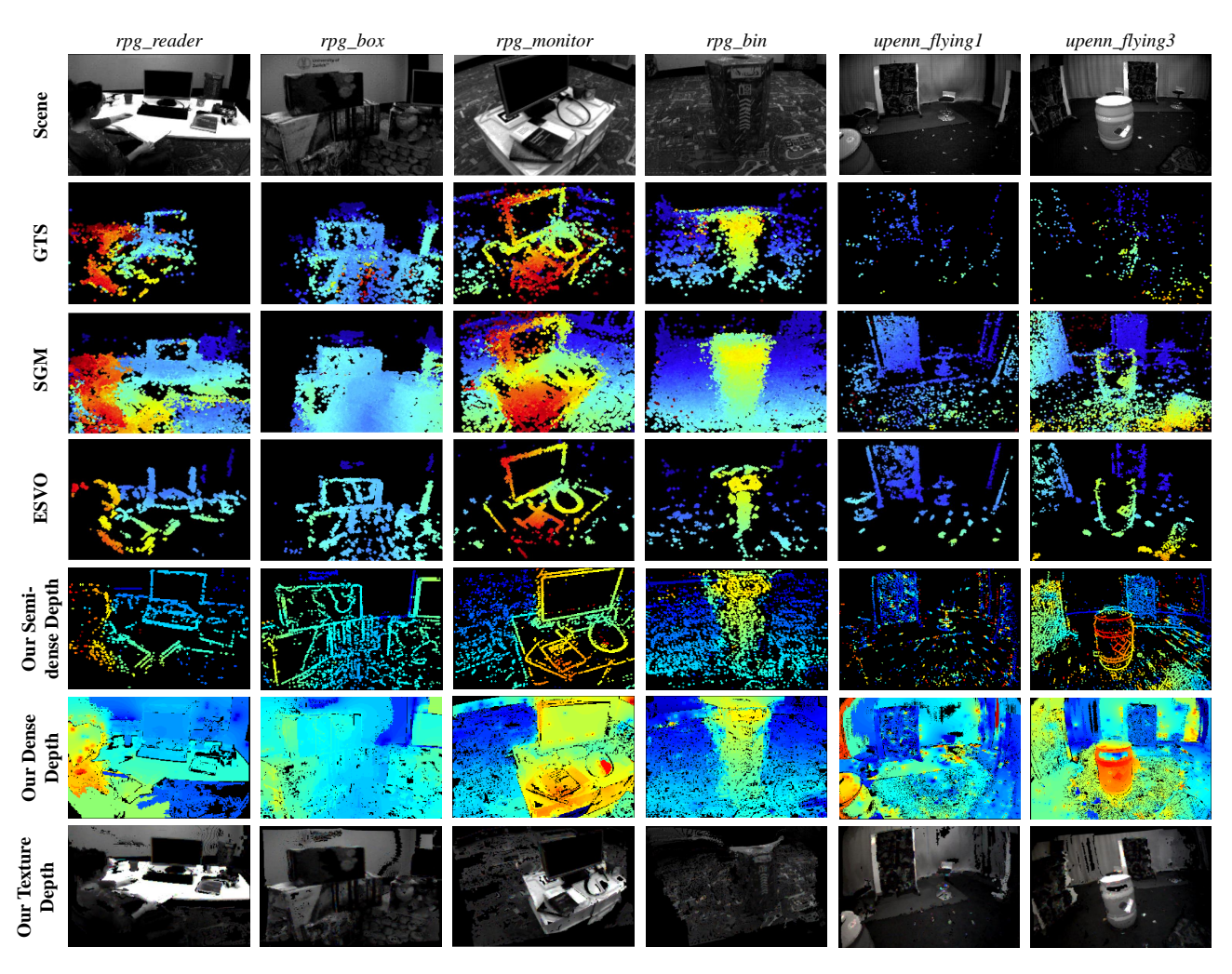


Fig. 9. Mapping result comparison. The first row shows the intensity frames from the event camera. Rows 2 to 4 show semi-depth estimation results from GTS [12], [65], SGM [12], [66], and ESVO [12], respectively. The last three rows show the estimated semi-dense depth, dense depth, and texture point cloud from our method. Depth maps are pseudo-colored, from red (close) to blue (far), in the range of 0.55-6.25 m for the rpg [3] and in the range 1.0-6.5 m for MVSEC [63].

unsuccessful. For instance, the sky areas in the illustrations correspond to regions that are too far for depth recovery. Additionally, certain textureless regions of the road, lacking sufficient event data, may also pose challenges for recovering dense depth. However, it is essential to recognize that such occurrences are inherent characteristics of event cameras. While these situations would not occur when operating indoors, our event-based dense mapping effectively recovers the complete dense depth along with the details of the structure. For instance, as illustrated in Fig. 8(c), our method adeptly reconstructs the texture of the poster, and the consistency of the wall depth is excellent. On the flat wall surface, most areas in our event-based dense map display similar colors, representing proximity and uniform distances across those regions.

C. Mapping Performance Comparison with Baselines

1) Qualitative Comparison: In this section, we conduct comparisons with other event-based depth estimation approaches using sequences from the MVSEC [63] and rpg [3]

dataset. Fig. 9 shows the inverse depth maps produced by our EVI-SAM and the baseline methods. The first row displays the raw image of the selected reference view. The second to the fourth row show inverse depth maps generated by GTS [12], [65], SGM [12], [66], and ESVO [12], respectively. The last three rows present the semi-dense, dense, and textured depth generated by our EVI-SAM. As anticipated, since event cameras solely respond to the apparent motion of edges, the methods that produce semi-dense depth maps can only depict edges of the 3D scene. In contrast, our EVI-SAM can recover texture and surface information to obtain dense depth maps. The results of GTS [12], [65], SGM [12], [66], and ESVO [12] are borrowed from the respective papers. For comparison, we select the reference views that are similar to the ones used in ESVO [12]. It is worth noting that, unlike our method, the baseline methods exclusively rely on known camera poses provided by an external motion capture system to run the mapping process. In contrast, our mapping approach relies on the pose feedback provided by our event-based hybrid tracking modules to achieve depth estimation. Additionally, our EVI-SAM utilizes a monocular event camera, while the baseline methods employ stereo event cameras. However, it still can be observed that our event-based mapping method gives the best results in terms of the overall depth recovery performance and density.

2) Quantitative Comparison: Table III details the depth errors associated with various event-based depth estimation methods in the MVSEC [63] flying drone sequences. We utilize mean depth error as our evaluation metric, computed by comparing estimated depth values with the ground truth depth obtained through 3D LiDAR. For the semi-dense methods, we validate them using their open-source code and known camera poses provided by the dataset. We choose estimated depths from each baseline that closely match the same ground truth depth for assessment. To ensure a fair comparison, we assign zero values to regions where depths fail to recover and calculate the density percentage of the semi-dense depth estimates. This enables the comparison with the dense ground truth depth. As can be seen from the results, our method performs better than these baselines in terms of dense depth recovery. To our knowledge, this is the first successful attempt to compute monocular dense depth results for event cameras without using learningbased methods. Note that the reported results of these eventbased semi-dense methods are inferior to those presented in original papers. This discrepancy is attributed to the usage of ground truth dense depth rather than ground truth sparse depth. Meanwhile, it should be noted that the ground truth dense depth provided by MVSEC may not be sufficiently accurate. Firstly, the low frequency of the ground truth depth poses a challenge to time alignment, particularly during camera motion. Secondly, errors in the ground truth depth could be introduced during the generation process, stemming from the odometry procedure. This may cause objects in the ground truth depth to appear inflated compared to their original versions in the image/event space. These factors constrain the ability to achieve accurate validation of mapping performance.

TABLE III. Quantitative comparison of mapping performance in terms of mean depth error (m) and the density percentage of the recovery (%), which is assessed against the dense ground truth depth.

Methods	Types		indoor_flying2			
Michigas		Mean Error(m) / Density Percentage (%)				
EMVS [2]	Mono	2.38 / 6.01%	1.82 / 4.90%	2.82 / 4.93%		
Ref. [4]	Stereo	2.46 / 1.79%	1.85 / 1.35%	2.88 / 1.85%		
ESVO [12]	Stereo	2.43 / 3.29%	1.80 / 4.00%	2.88 / 2.34%		
Ours	Mono	0.78 / 100%	0.82 / 100%	0.86 / 100%		

D. Mapping Performance in Challenge Situations

The tracking performance of our EVI-SAM in the scenarios involving aggressive motion and HDR has been effectively evaluated in Section VI-A. In this section, we specifically evaluate the mapping performance of our EVI-SAM in challenging conditions.

1) Mapping Performance in HDR: In this experiment, we demonstrate the effectiveness of our event-based dense

mapping in HDR scenarios using an event-based driving dataset (ECMD [67]). We specifically choose three sequences (Dense urban, Tunnel, and Suburban road) that exhibit HDR scenes caused by the intense illumination change. Fig. 10 illustrates the successful recovery of dense depth by our event-based dense mapping under challenging conditions, including intense sunlight and HDR encountered in tunnels. Besides, as shown in Fig. 8(k), our event-based dense mapping is capable of recovering dense depth even in low-light scenarios. Despite these achievements, addressing nighttime driving scenarios proves to be a significant challenge. This challenge arises from the expansive and dark characteristics of nighttime driving environments. Our event-based dense point cloud derives texture information from image measurements, resulting in the point cloud that appears pitch-black in such conditions. In conclusion, our event-based dense mapping remains effective in recovering depth under HDR scenarios. Nevertheless, it is crucial to acknowledge that HDR conditions may impact the texture of our dense point cloud.

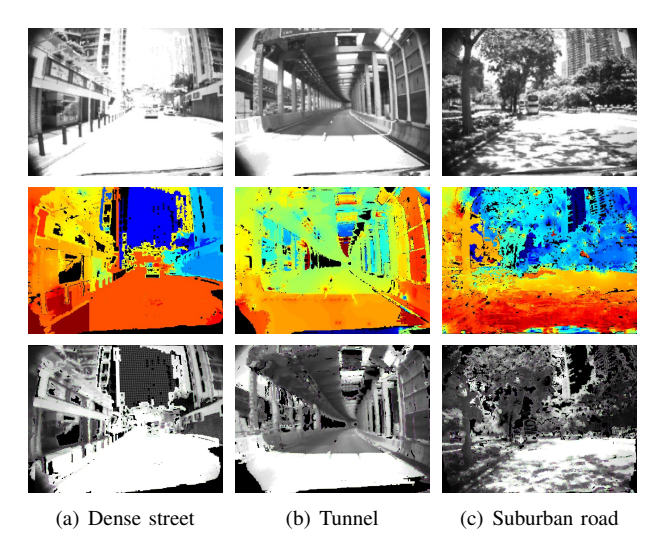


Fig. 10. Mapping result of EVI-SAM under HDR scenes. The first row shows the intensity frames from the event camera. The second row shows the event-based dense map, and the last row is the event-based dense point cloud with texture information. Since the texture information is adopted from the image measurement, the event-based dense point cloud exhibits overexposure caused by strong sunlight. While our event-based dense map would not be affected by the illumination.

2) Mapping Performance in Aggressive Motions: In this experiment, we examine the robustness of our event-based dense mapping in scenarios involving aggressive motions (see Fig. 11), where the maximum angular velocity reaches up to $5 \ rad/s$ (approximately $290^\circ/s$), and the linear acceleration reaches up to $18 \ m^2/s$ (see the gyroscope and acceleration readings in the left part of Fig. 11). The results of our estimated event-based dense depth and texture point cloud are also presented alongside timestamps, with the aggressive motion phase shaded in grey blocks. It can be

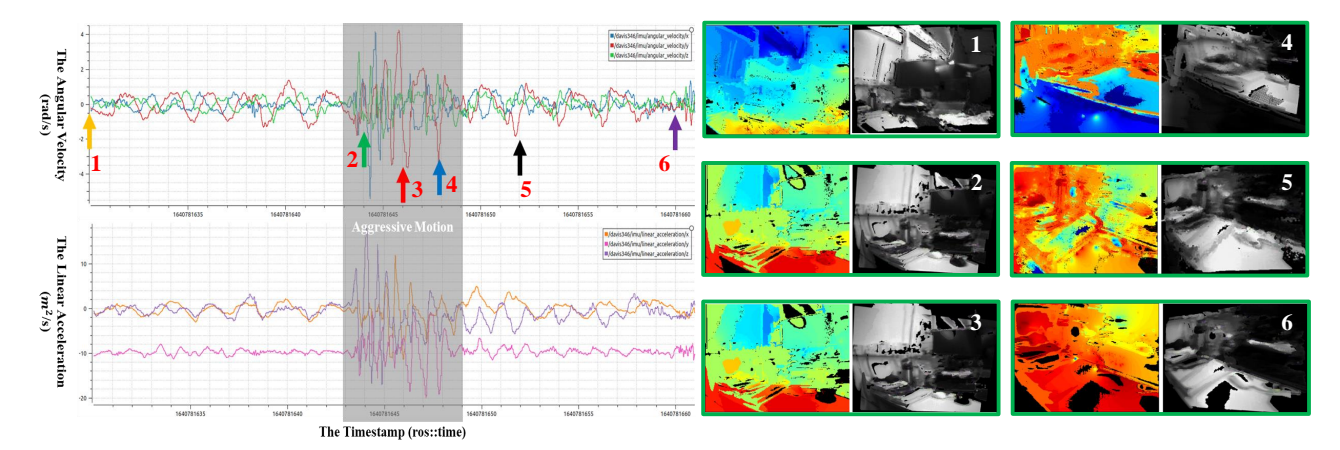


Fig. 11. Mapping result of EVI-SAM under aggressive motions. We visualize the result of our event-based dense mapping along with the timestamp (ROS time), and the raw gyroscope and acceleration reading from the IMU. The shaded area in grey represents the phase of aggressive motions.

observed that our event-based dense mapping consistently and stably reconstructs the 3D structure of the scene even in the presence of intense rotation and translation motions. These results underscore the robustness of our algorithm and demonstrate its capacity to handle scenarios with aggressive motions. For visual demonstrations of our mapping results under aggressive motions, please refer to the supplementary video.

E. Full System Onboard Evaluation

Although the data sequence utilized in the previous section is appropriate for assessing the performance of pose tracking and mapping in challenging situations, it does not encompass real-time onboard evaluation and global mapping. Moreover, we lack a dataset for comparing our event-based dense mapping with the depth camera. To fill this gap, we design an event-based handheld device and evaluate the onboard performance of our EVI-SAM. Please note that the depth maps provided by the depth camera only serve as references for qualitative comparison.

1) Event-based Handheld Device: Our handheld device is shown in Fig. 12, which includes a power supply unit, an onboard computer NUC (equipped with Intel i7-1260P, 32GB RAM, and Ubuntu 20.04 operation system), a DAVIS346 event camera, and a Intel® RealSenseTM D455 RGB-D camera. All mechanical modules of this device are designed for 3D printing, and both design schematics and the collected data sequence are available on our GitHub repository: https://github.com/arclab-hku/Event_based_VO-VIO-SLAM?tab=readme-ov-file#5-evi-sam

2) Local Mapping Performance: We conduct real-time testing of EVI-SAM using the handheld device within the LG01_lab of the Haking Wong Building at The University of Hong Kong. The results, including event-based dense mapping at selected viewpoints and the estimated trajectory, are illustrated in Fig. 14. Three live demonstrations are also available in the supplemental video. Additionally, we conducted qualitative comparisons between the dense mapping results from our EVI-SAM and the depth images

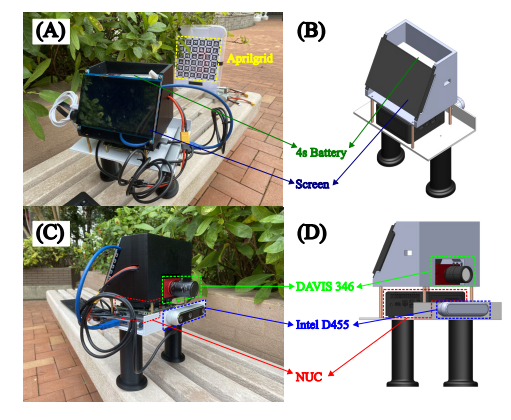


Fig. 12. The event-based handheld device with the schematics model for onboard evaluation. Please note that the RGB-D camera (Intel D455) is only used for reference, the complete system of our EVI-SAM operates exclusively with the monocular event camera (DAVIS346).

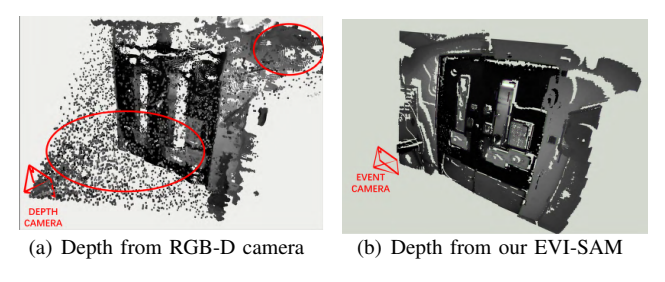


Fig. 13. Comparing the local texture depth generated by EVI-SAM with the one produced by the RGB-D camera.

from the RGB-D camera. To ensure a fair comparison, we render the texture information from the intensity image of DAVIS346 onto the depth image of the RGB-D camera, maintaining the same resolution as the DAVIS346. The depth images are directly acquired from the RGB-D camera, with its infrared ranging sensor obscured. We directly align the texture point cloud from the RGB-D camera along with the estimated pose of our tracking module. As observed in the highlighted area within the red circle in Fig. 13,

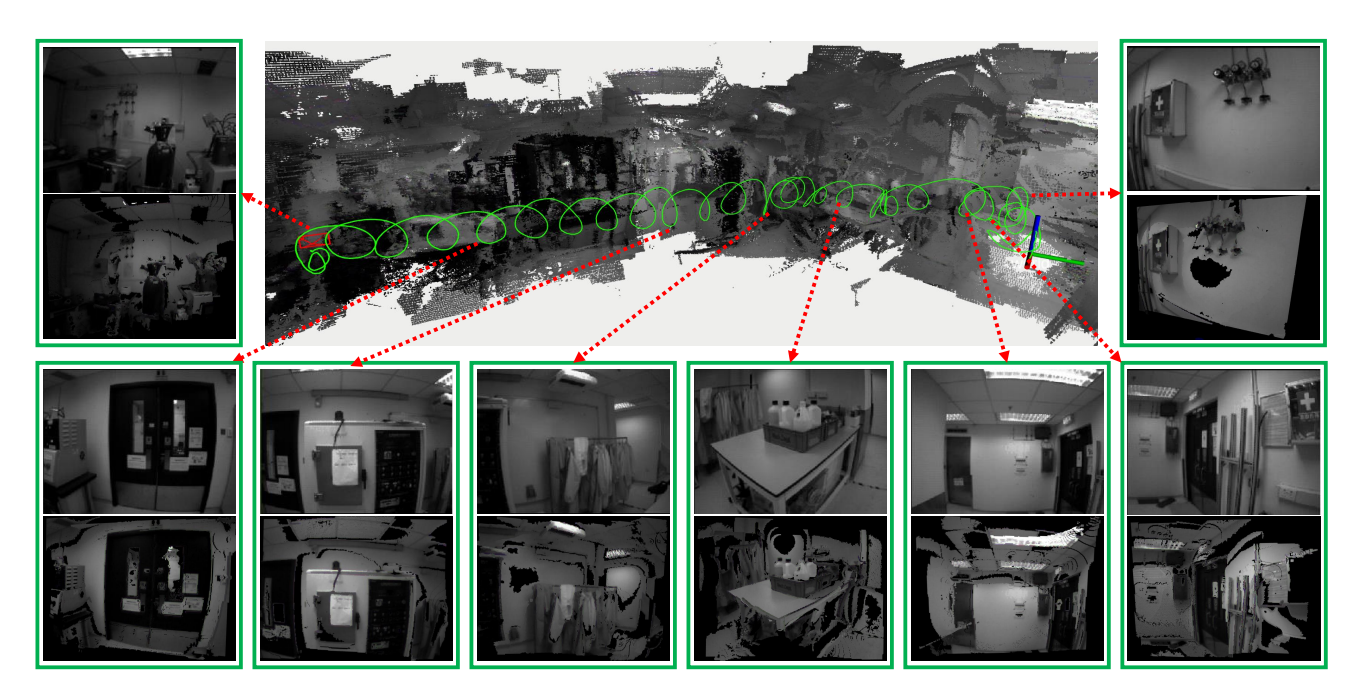


Fig. 14. Visualization of the estimated camera trajectory and global 3D reconstruction (surface mesh) of our EVI-SAM. Sequentially display from right to left includes the event-based dense point cloud with texture information and the intensity image, at selected viewpoints.

it is evident that the local depth map generated by the RGB-D camera exhibits more noise than that of our EVI-SAM. Our proposed event-based dense mapping approach demonstrates performance comparable to commercial depth cameras. Moreover, it exhibits superior noise reduction and texture recovery capabilities.

3) Global Mapping Performance: The global mapping performance of our EVI-SAM is also illustrated in Fig. 14, showing the surface mesh generated through TSDF-based map fusion. Our global event-based dense mapping exhibits excellent global consistency. Three live demonstrations are available at https://b23.tv/cwetpxL, illustrating our incremental reconstruction of the event-based surface mesh from updated TSDF voxels. This process enables on-demand meshing for visualization, allowing flexibility in generating the mesh at any time. Our TSDF-based map fusion for global mapping is designed to generate surface meshes that enable humans to assess the 3D reconstructed environment more effectively. This capability supports high-level mission goals, such as collision-free motion planning. During evaluation, an onboard computer NUC is utilized to support real-time pose estimation and local event-based dense mapping. However, the NUC lacks sufficient computational power to support a real-time meshing process. Therefore, we utilize a more powerful processor (Intel i7-11800H, 32GB RAM) without GPU to output the global mesh of EVI-SAM during the evaluation. Further details regarding the time-consuming aspects of different modules will be discussed in Section VI-F.

F. Running Time Analysis

In this section, we investigate the average time consumption of our proposed system on the CPU-only NUC. We

calculate the average time consumption during the evaluation of Section VI-E, whose results are shown in Table IV. The hybrid tracking module takes an average of 55.24 ms with an additional 3.75 ms for event-corner feature tracking, and the dense mapping module takes an average of 137.45 ms processing time. The estimated pose frequency can be effort-lessly boosted to IMU-rate by directly integrating the latest estimation with IMU measurements in a loosely-coupled manner. Meanwhile, the dense map generation frequency is around 7 Hz, which should be real-time enough for tasks like collision-free motion planning, e.g. obstacle avoidance.

TABLE IV. The average time consumption of different modules in our EVI-SAM

Sequence	Event-corner tracking Mean / Std (ms)	Hybrid tracking Mean / Std (ms)	Dense mapping Mean / Std (ms)
Logo_wall_1	3.50 / 1.17	54.39 / 23.35	138.21 / 79.49
Logo_wall_2	3.75 / 1.03	55.11 / 23.01	123.8 / 49.24
LG_Factory	4.49 / 1.66	67.29 / 54.90	129.63 / 44.54
LG_office	3.89 / 1.37	55.10 / 31.88	112.09 / 40.96
Fountain_1	3.75 / 1.15	49.78 / 15.76	141.46 / 48.59
Fountain_2	3.11 / 1.14	49.79 / 8.57	179.49 / 106.68
Average	3.75 / 1.25	55.24 / 26.24	137.45 / 61.57

G. Limitations and Discussions

Regarding our event-based hybrid pose tracking, although it can provide robust and accurate state estimation results under challenging situations such as fast motion and HDR, the produced estimates of the pose are in a discrete manner. In future work, we might further explore the trajectory of the camera pose as a continuous-time entity.

Regarding our event-based dense mapping, one limitation lies in the difficulty of attaining comprehensive and precise recovery of dense depth across various environments. This is caused by two primary factors. The first factor is the inherent nature of event cameras, which produce sparse pixels and only respond to moving edges. The second factor is attributed to scenes being too distant from the camera, such as the sky in a driving scenario. Conversely, when the event camera operates in structured environments where depth patterns exhibit regularity, such as many planar surfaces with limited edges, or scenarios with sharp object boundaries, our method can leverage this regularity to infer good dense depth from a small number of event measurements. Besides, our event-based dense mapping is a kind of color-guided depth enhancement method. This kind of approach is under the assumption that the edges of the event-based semi-dense depth and the color edges at the corresponding locations are consistent. Therefore, the incorrect guidance from the companion color image will lead to texture-copy artifacts and blurring depth edges on the reconstructed dense depth. While various methods [68], [69] exist to address this issue, we intend to defer this challenge to future works.

Another limitation of our event-based dense mapping is the inevitable occurrence of artifacts. The term "artifacts" pertains to specific errors in scale recovery, such as cases where small areas in distant regions are mistakenly reconstructed as closer ones. This could be attributed to the implementation of the monocular MVS problem in our approach, resulting in a loss of scale. Consequently, in future work, we may extend our algorithm to incorporate stereo vision to address this issue.

Regarding effectively utilizing image information for event-based dense mapping, we incorporate image segmentation to guide the inference of event-based dense depth within each segmented region. This approach goes beyond solely relying on texture information to generate colorful dense maps. Hence, the adoption of a suitable image segmentation strategy, structural integrity of semi-dense recovery, and the removal of outliers become crucial for enhancing the performance of our dense mapping. Apart from using the image as guidance through traditional segmentation or Canny edge extraction methods, there exists a plethora of depth completion methods, such as learning-based approaches [70], [71], Markov Random Field (MRF) methods [72], etc. We hope this work can serve as inspiration for the research community, encouraging a shift away from only learning dense depth from sparse events. Instead, we advocate for leveraging intensity images to provide complementary or guiding information, such as scene structure or texture, to complement the missing cues of sparse events.

VII. CONCLUSIONS

In this paper, we presented EVI-SAM, a framework designed for 6 DoF pose tracking and 3D dense mapping using monocular event camera. To enhance the robustness and accuracy of 6-DoF pose tracking, we proposed the first event-based hybrid pose tracking framework which combines the robustness of feature-based event pose tracking with the relatively high accuracy achieved through event-based direct alignment. To achieve dense mapping, we

proposed an image-guided and segmentation-based approach to reconstruct dense maps from sparse and incomplete event measurements. To create a comprehensive representation of the 3D environment, we designed TSDF-based map fusion to construct both the textured global map and the surface mesh. Our framework balances accuracy and robustness against computational efficiency towards strong tracking and mapping performance in challenging scenarios such as HDR or fast motion. Notably, EVI-SAM demonstrates computational efficiency for real-time execution, making it suitable for onboard localization, mapping, and navigation. Meanwhile, the generated event-based dense map can be directly applied to collision-free motion planning, ensuring safe navigation. In future work, we aim to explore a full event-based navigation and obstacle avoidance system based on our EVI-SAM.

REFERENCES

- [1] G. Gallego, T. Delbrück, G. Orchard, C. Bartolozzi, B. Taba, A. Censi, S. Leutenegger, A. J. Davison, J. Conradt, K. Daniilidis, et al., "Eventbased vision: A survey," *IEEE transactions on pattern analysis and* machine intelligence, vol. 44, no. 1, pp. 154–180, 2020.
- [2] H. Rebecq, G. Gallego, E. Mueggler, and D. Scaramuzza, "Emvs: Event-based multi-view stereo—3d reconstruction with an event camera in real-time," *International Journal of Computer Vision*, vol. 126, no. 12, pp. 1394–1414, 2018.
- [3] Y. Zhou, G. Gallego, H. Rebecq, L. Kneip, H. Li, and D. Scaramuzza, "Semi-dense 3d reconstruction with a stereo event camera," in *Proceedings of the European conference on computer vision (ECCV)*, 2018, pp. 235–251.
- [4] S. Ghosh and G. Gallego, "Multi-event-camera depth estimation and outlier rejection by refocused events fusion," *Advanced Intelligent Systems*, vol. 4, no. 12, p. 2200221, 2022.
- [5] A. Z. Zhu, L. Yuan, K. Chaney, and K. Daniilidis, "Unsupervised event-based learning of optical flow, depth, and egomotion," in Proceedings of the IEEE/CVF Conference on Computer Vision and Pattern Recognition, 2019, pp. 989–997.
- [6] V. Rudnev, M. Elgharib, C. Theobalt, and V. Golyanik, "Eventnerf: Neural radiance fields from a single colour event camera," in *Proceedings of the IEEE/CVF Conference on Computer Vision and Pattern Recognition*, 2023, pp. 4992–5002.
- [7] S. Tulyakov, F. Fleuret, M. Kiefel, P. Gehler, and M. Hirsch, "Learning an event sequence embedding for dense event-based deep stereo," in Proceedings of the IEEE/CVF International Conference on Computer Vision, 2019, pp. 1527–1537.
- [8] Y. Nam, M. Mostafavi, K.-J. Yoon, and J. Choi, "Stereo depth from events cameras: Concentrate and focus on the future," in *Proceedings of the IEEE/CVF Conference on Computer Vision and Pattern Recognition*, 2022, pp. 6114–6123.
- [9] S. H. Ahmed, H. W. Jang, S. N. Uddin, and Y. J. Jung, "Deep event stereo leveraged by event-to-image translation," in *Proceedings of the AAAI Conference on Artificial Intelligence*, vol. 35, no. 2, 2021, pp. 882–890.
- [10] M. Mostafavi, K.-J. Yoon, and J. Choi, "Event-intensity stereo: Estimating depth by the best of both worlds," in *Proceedings of the IEEE/CVF International Conference on Computer Vision*, 2021, pp. 4258–4267.
- [11] H. Rebecq, T. Horstschäfer, G. Gallego, and D. Scaramuzza, "Evo: A geometric approach to event-based 6-dof parallel tracking and mapping in real time," *IEEE Robotics and Automation Letters*, vol. 2, no. 2, pp. 593–600, 2016.
- [12] Y. Zhou, G. Gallego, and S. Shen, "Event-based stereo visual odometry," *IEEE Transactions on Robotics*, 2021.
- [13] J. Hidalgo-Carrió, G. Gallego, and D. Scaramuzza, "Event-aided direct sparse odometry," in *Proceedings of the IEEE/CVF Conference* on Computer Vision and Pattern Recognition, 2022, pp. 5781–5790.
- [14] A. R. Vidal, H. Rebecq, T. Horstschaefer, and D. Scaramuzza, "Ultimate slam? combining events, images, and imu for robust visual slam in hdr and high-speed scenarios," *IEEE Robotics and Automation Letters*, vol. 3, no. 2, pp. 994–1001, 2018.

- [15] W. Guan, P. Chen, Y. Xie, and P. Lu, "Pl-evio: Robust monocular event-based visual inertial odometry with point and line features," *IEEE Transactions on Automation Science and Engineering*, 2023.
- [16] P. Chen, W. Guan, and P. Lu, "Esvio: Event-based stereo visual inertial odometry," *IEEE Robotics and Automation Letters*, vol. 8, no. 6, pp. 3661–3668, 2023.
- [17] A. Zihao Zhu, N. Atanasov, and K. Daniilidis, "Event-based visual inertial odometry," in *Proceedings of the IEEE Conference on Computer Vision and Pattern Recognition*, 2017, pp. 5391–5399.
- [18] H. Rebecq, T. Horstschaefer, and D. Scaramuzza, "Real-time visual-inertial odometry for event cameras using keyframe-based nonlinear optimization," in *British Machine Vision Conference (BMVC)*, 2017.
- [19] E. Mueggler, G. Gallego, H. Rebecq, and D. Scaramuzza, "Continuous-time visual-inertial odometry for event cameras," *IEEE Transactions on Robotics*, vol. 34, no. 6, pp. 1425–1440, 2018.
- [20] F. Mahlknecht, D. Gehrig, J. Nash, F. M. Rockenbauer, B. Morrell, J. Delaune, and D. Scaramuzza, "Exploring event camera-based odometry for planetary robots," *IEEE Robotics and Automation Letters (RA-L)*, 2022.
- [21] D. Gehrig, H. Rebecq, G. Gallego, and D. Scaramuzza, "Eklt: Asynchronous photometric feature tracking using events and frames," *International Journal of Computer Vision*, vol. 128, no. 3, pp. 601–618, 2020.
- [22] W. Guan and P. Lu, "Monocular event visual inertial odometry based on event-corner using sliding windows graph-based optimization," in 2022 IEEE/RSJ International Conference on Intelligent Robots and Systems (IROS). IEEE, 2022, pp. 2438–2445.
- [23] B. Dai, C. L. Gentil, and T. Vidal-Calleja, "A tightly-coupled eventinertial odometry using exponential decay and linear preintegrated measurements," in 2022 IEEE/RSJ International Conference on Intelligent Robots and Systems (IROS), 2022, pp. 9475–9482.
- [24] D. Liu, A. Parra, Y. Latif, B. Chen, T.-J. Chin, and I. Reid, "Asynchronous optimisation for event-based visual odometry," in 2022 International Conference on Robotics and Automation (ICRA). IEEE, 2022, pp. 9432–9438.
- [25] C. Le Gentil, F. Tschopp, I. Alzugaray, T. Vidal-Calleja, R. Siegwart, and J. Nieto, "Idol: A framework for imu-dvs odometry using lines," in 2020 IEEE/RSJ International Conference on Intelligent Robots and Systems (IROS). IEEE, 2020, pp. 5863–5870.
- [26] W. Chamorro, J. Solà, and J. Andrade-Cetto, "Event-imu fusion strategies for faster-than-imu estimation throughput," in *Proceedings of the IEEE/CVF Conference on Computer Vision and Pattern Recognition*, 2023, pp. 3975–3982.
- [27] W. Chamorro, J. Solà, and J. Andrade-Cetto, "Event-based line slam in real-time," *IEEE Robotics and Automation Letters*, vol. 7, no. 3, pp. 8146–8153, 2022.
- [28] H. Kim, S. Leutenegger, and A. J. Davison, "Real-time 3d reconstruction and 6-dof tracking with an event camera," in *European Conference on Computer Vision*. Springer, 2016, pp. 349–364.
- [29] G. Gallego, J. E. Lund, E. Mueggler, H. Rebecq, T. Delbruck, and D. Scaramuzza, "Event-based, 6-dof camera tracking from photometric depth maps," *IEEE transactions on pattern analysis and machine* intelligence, vol. 40, no. 10, pp. 2402–2412, 2017.
- [30] S. Bryner, G. Gallego, H. Rebecq, and D. Scaramuzza, "Event-based, direct camera tracking from a photometric 3d map using nonlinear optimization," in 2019 International Conference on Robotics and Automation (ICRA). IEEE, 2019, pp. 325–331.
- [31] Y.-F. Zuo, J. Yang, J. Chen, X. Wang, Y. Wang, and L. Kneip, "Devo: Depth-event camera visual odometry in challenging conditions," in 2022 International Conference on Robotics and Automation (ICRA). IEEE, 2022, pp. 2179–2185.
- [32] Y. Dong, "Standardand event cameras fusion for dense mapping," arXiv preprint arXiv:2102.03567, 2021.
- [33] H. Cho, J. Jeong, and K.-J. Yoon, "Eomvs: Event-based omnidirectional multi-view stereo," *IEEE Robotics and Automation Letters*, vol. 6, no. 4, pp. 6709–6716, 2021.
- [34] G. Gallego, H. Rebecq, and D. Scaramuzza, "A unifying contrast maximization framework for event cameras, with applications to motion, depth, and optical flow estimation," in *Proceedings of the IEEE conference on computer vision and pattern recognition*, 2018, pp. 3867–3876.
- [35] S. Chiavazza, S. M. Meyer, and Y. Sandamirskaya, "Low-latency monocular depth estimation using event timing on neuromorphic hardware," in *Proceedings of the IEEE/CVF Conference on Computer* Vision and Pattern Recognition, 2023, pp. 4070–4079.

- [36] K. Chaney, A. Zihao Zhu, and K. Daniilidis, "Learning event-based height from plane and parallax," in *Proceedings of the IEEE/CVF* Conference on Computer Vision and Pattern Recognition Workshops, 2019, pp. 0–0.
- [37] J. Hidalgo-Carrió, D. Gehrig, and D. Scaramuzza, "Learning monocular dense depth from events," in 2020 International Conference on 3D Vision (3DV). IEEE, 2020, pp. 534–542.
- [38] D. Gehrig, M. Rüegg, M. Gehrig, J. Hidalgo-Carrió, and D. Scaramuzza, "Combining events and frames using recurrent asynchronous multimodal networks for monocular depth prediction," *IEEE Robotics and Automation Letters*, vol. 6, no. 2, pp. 2822–2829, 2021.
- [39] I. Hwang, J. Kim, and Y. M. Kim, "Ev-nerf: Event based neural radiance field," in *Proceedings of the IEEE/CVF Winter Conference* on Applications of Computer Vision, 2023, pp. 837–847.
- [40] S. Klenk, L. Koestler, D. Scaramuzza, and D. Cremers, "E-nerf: Neural radiance fields from a moving event camera," *IEEE Robotics and Automation Letters*, vol. 8, no. 3, pp. 1587–1594, 2023.
- [41] S. Mahbub, B. Feng, and C. Metzler, "Multimodal neural surface reconstruction: Recovering the geometry and appearance of 3d scenes from events and grayscale images," in *NeurIPS 2023 Workshop on Deep Learning and Inverse Problems*, 2023.
- [42] S.-H. Ieng, J. Carneiro, M. Osswald, and R. Benosman, "Neuromorphic event-based generalized time-based stereovision," *Frontiers in Neuroscience*, vol. 12, p. 442, 2018.
- [43] Z. Liu, D. Shi, R. Li, Y. Zhang, and S. Yang, "T-esvo: Improved event-based stereo visual odometry via adaptive time-surface and truncated signed distance function," *Advanced Intelligent Systems*, p. 2300027, 2023.
- [44] S. Ghosh and G. Gallego, "Event-based stereo depth estimation from ego-motion using ray density fusion," *European Conf. on Computer Vision Workshops (ECCVW) Ego4D*, 2022.
- [45] J. Engel, V. Koltun, and D. Cremers, "Direct sparse odometry," *IEEE transactions on pattern analysis and machine intelligence*, vol. 40, no. 3, pp. 611–625, 2017.
- [46] K. Huang, S. Zhang, J. Zhang, and D. Tao, "Event-based simultaneous localization and mapping: A comprehensive survey," arXiv preprint arXiv:2304.09793, 2023.
- [47] C. Forster, Z. Zhang, M. Gassner, M. Werlberger, and D. Scaramuzza, "Svo: Semidirect visual odometry for monocular and multicamera systems," *IEEE Transactions on Robotics*, vol. 33, no. 2, pp. 249– 265, 2016.
- [48] J. H. Jung, Y. Choe, and C. G. Park, "Photometric visual-inertial navigation with uncertainty-aware ensembles," *IEEE Transactions on Robotics*, vol. 38, no. 4, pp. 2039–2052, 2022.
- [49] R. T. Collins, "A space-sweep approach to true multi-image matching," in *Proceedings CVPR IEEE Computer Society Conference on Computer Vision and Pattern Recognition*. Ieee, 1996, pp. 358–363.
- [50] F. Ma, L. Carlone, U. Ayaz, and S. Karaman, "Sparse depth sensing for resource-constrained robots," *The International Journal of Robotics Research*, vol. 38, no. 8, pp. 935–980, 2019.
- [51] H.-T. Zhang, J. Yu, and Z.-F. Wang, "Probability contour guided depth map inpainting and superresolution using non-local total generalized variation," *Multimedia Tools and Applications*, vol. 77, pp. 9003– 9020, 2018.
- [52] K. Wang, W. Ding, and S. Shen, "Quadtree-accelerated real-time monocular dense mapping," in 2018 IEEE/RSJ International Conference on Intelligent Robots and Systems (IROS). IEEE, 2018, pp. 1–9.
- [53] A. Telea, "An image inpainting technique based on the fast marching method," *Journal of graphics tools*, vol. 9, no. 1, pp. 23–34, 2004.
- [54] M. Nießner, M. Zollhöfer, S. Izadi, and M. Stamminger, "Real-time 3d reconstruction at scale using voxel hashing," ACM Transactions on Graphics (ToG), vol. 32, no. 6, pp. 1–11, 2013.
- [55] H. Oleynikova, Z. Taylor, M. Fehr, R. Siegwart, and J. Nieto, "Voxblox: Incremental 3d euclidean signed distance fields for onboard may planning," in 2017 IEEE/RSJ International Conference on Intelligent Robots and Systems (IROS). IEEE, 2017, pp. 1366–1373.
- [56] E. Mueggler, H. Rebecq, G. Gallego, T. Delbruck, and D. Scaramuzza, "The event-camera dataset and simulator: Event-based data for pose estimation, visual odometry, and slam," *The International Journal of Robotics Research*, vol. 36, no. 2, pp. 142–149, 2017.
- [57] I. Alzugaray and M. Chli, "Asynchronous multi-hypothesis tracking of features with event cameras," in 2019 International Conference on 3D Vision (3DV). IEEE, 2019, pp. 269–278.
- [58] B. Dai, C. Le Gentil, and T. Vidal-Calleja, "A tightly-coupled eventinertial odometry using exponential decay and linear preintegrated

- measurements," in 2022 IEEE/RSJ International Conference on Intelligent Robots and Systems (IROS). IEEE, 2022, pp. 9475–9482.
- [59] M. S. Lee, J. H. Jung, Y. J. Kim, and C. G. Park, "Event-and frame-based visual-inertial odometry with adaptive filtering based on 8-dof warping uncertainty," *IEEE Robotics and Automation Letters*, 2023.
- [60] C. Campos, R. Elvira, J. J. G. Rodríguez, J. M. Montiel, and J. D. Tardós, "Orb-slam3: An accurate open-source library for visual, visual-inertial, and multimap slam," *IEEE Transactions on Robotics*, 2021.
- [61] T. Qin, P. Li, and S. Shen, "Vins-mono: A robust and versatile monocular visual-inertial state estimator," *IEEE Transactions on Robotics*, vol. 34, no. 4, pp. 1004–1020, 2018.
- [62] L. Gao, Y. Liang, J. Yang, S. Wu, C. Wang, J. Chen, and L. Kneip, "Vector: A versatile event-centric benchmark for multi-sensor slam," *IEEE Robotics and Automation Letters*, 2022.
- [63] A. Z. Zhu, D. Thakur, T. Özaslan, B. Pfrommer, V. Kumar, and K. Daniilidis, "The multivehicle stereo event camera dataset: An event camera dataset for 3d perception," *IEEE Robotics and Automation Letters*, vol. 3, no. 3, pp. 2032–2039, 2018.
- [64] M. Gehrig, W. Aarents, D. Gehrig, and D. Scaramuzza, "Dsec: A stereo event camera dataset for driving scenarios," *IEEE Robotics and Automation Letters*, vol. 6, no. 3, pp. 4947–4954, 2021.
- [65] S.-H. Ieng, J. Carneiro, M. Osswald, and R. Benosman, "Neuromorphic event-based generalized time-based stereovision," *Frontiers in neuroscience*, vol. 12, p. 442, 2018.
- [66] H. Hirschmuller, "Stereo processing by semiglobal matching and mutual information," *IEEE Transactions on pattern analysis and machine intelligence*, vol. 30, no. 2, pp. 328–341, 2007.
- [67] P. Chen, W. Guan, F. Huang, Y. Zhong, W. Wen, L.-T. Hsu, and P. Lu, "Ecmd: An event-centric multisensory driving dataset for slam," *IEEE Transactions on Intelligent Vehicles*, 2023.
- [68] O. Choi and S.-W. Jung, "A consensus-driven approach for structure and texture aware depth map upsampling," *IEEE transactions on image processing*, vol. 23, no. 8, pp. 3321–3335, 2014.
 [69] S. Xiang, L. Yu, and C. W. Chen, "No-reference depth assessment
- [69] S. Xiang, L. Yu, and C. W. Chen, "No-reference depth assessment based on edge misalignment errors for t+ d images," *IEEE Transactions on Image Processing*, vol. 25, no. 3, pp. 1479–1494, 2015.
- [70] B. Bescos, J. M. Fácil, J. Civera, and J. Neira, "Dynaslam: Tracking, mapping, and inpainting in dynamic scenes," *IEEE Robotics and Automation Letters*, vol. 3, no. 4, pp. 4076–4083, 2018.
- [71] J. Hu, C. Bao, M. Ozay, C. Fan, Q. Gao, H. Liu, and T. L. Lam, "Deep depth completion from extremely sparse data: A survey," *IEEE Transactions on Pattern Analysis and Machine Intelligence*, 2022.
- [72] J. Zhu, L. Wang, J. Gao, and R. Yang, "Spatial-temporal fusion for high accuracy depth maps using dynamic mrfs," *IEEE Transactions* on *Pattern Analysis and Machine Intelligence*, vol. 32, no. 5, pp. 899– 909, 2009.



Guan Weipeng obtained his Bachelor degree in Electronic Science & Technology, as well as Master degree in Control Theory and Control Engineering from the South China University of Technology. He is currently pursuing his PhD degree in Robotics at the University of Hong Kong. He has worked with several reputable organizations, including: Samsung Electronics, Huawei Technologies, The Chinese Academy of Sciences, The Chinese University of Hong Kong, The Hong Kong University of Science and Technology, etc.

He has also served as a technical consultant for multiple companies, such as TCL. Moreover, he has published over 60 research articles in prestigious international journals and conferences, as well as holds more than 40 authorized patents. His research interests primarily focus on robotics, event-based VO/VIO/SLAM, visible light positioning, etc.



Chen Peiyu received the BSc degrees in automation from the Nanjing University of Science and Technology, China, and MSc degrees in computer control & automation from the Nanyang Technological University, Singapore, in 2020 and 2022, respectively. He is currently working forward the Ph.D. degree at the University of Hong Kong. His research interests include robotics, visual-inertial simultaneous localization and mapping, nonlinear control, and so on.



Zhao Huibin received the BSc degrees in aerospace engineering from Beihang University, China, and MSc degrees in Robotics from the University of Bristol, UK, in 2018 and 2020, respectively. He is currently working forward the Ph.D. degree at the University of Hong Kong. His research interests include robotics, learning-based 3D reconstruction, and so on.



Wang Yu received the BSc degrees in Mechanical Engineering from Auburn University, USA, and MSc degrees in Mechanical Engineering from the University of Hong Kong, in 2021 and 2023, respectively. He is currently working forward the MPhil degree at the University of Hong Kong.



Lu Peng obtained his BSc degree in automatic control and MSc degree in nonlinear flight control both from Northwestern Polytechnical University (NPU). He continued his journey on flight control at Delft University of Technology (TU Delft) where he received his PhD degree in 2016. After that, he shifted a bit from flight control and started to explore control for ground/construction robotics at ETH Zurich (ADRL lab) as a Postdoc researcher in 2016. He also had a short but nice journey at University of Zurich & ETH Zurich

(RPG group) where he was working on vision-based control for UAVs as a Postdoc researcher. He was an assistant professor in autonomous UAVs and robotics at Hong Kong Polytechnic University prior to joining the University of Hong Kong in 2020.

Prof. Lu has received several awards such as 3rd place in 2019 IROS autonomous drone racing competition and best graduate student paper finalist in AIAA GNC (top conference in aerospace). He serves as an associate editor for 2020 IROS (top conference in robotics) and session chair/co-chair for conferences like IROS and AIAA GNC for several times. He also gave a number of invited/keynote speeches at multiple conferences, universities and research institutes.